# 4 Rock strength and deformability

## 4.1 Introduction

The engineering mechanics-based approach to the solution of mining rock mechanics problems used in this book, requires prior definition of the stress–strain behaviour of the rock mass. Important aspects of this behaviour are the constants relating stresses and strains in the elastic range, the stress levels at which yield, fracturing or slip occurs within the rock mass, and the post-peak stress–strain behaviour of the fractured or 'failed' rock.

In some problems, it may be the behaviour of the **intact rock material** that is of concern. This will be the case when considering the excavation of rock by drilling and blasting, or when considering the stability of excavations in good quality, brittle rock which is subject to rockburst conditions. In other instances, the behaviour of **single discontinuities**, or of a small number of discontinuities, will be of paramount importance. Examples of this class of problem include the equilibrium of blocks of rock formed by the intersections of three or more discontinuities and the roof or wall of an excavation, and cases in which slip on a major throughgoing fault must be analysed. A different class of problem is that in which the rock mass must be considered as an assembly of **discrete blocks**. As noted in section 6.7 which describes the distinct element method of numerical analysis, the normal and shear force–displacement relations at block face-to-face and corner-to-face contacts are of central importance in this case. Finally, it is sometimes necessary to consider the global response of a **jointed rock mass** in which the discontinuity spacing is small on the scale of the problem domain. The behaviour of caving masses of rock is an obvious example of this class of problem.

It is important to note that the presence of major discontinuities or of a number of joint sets does not necessarily imply that the rock mass will behave as a discontinuum. In mining settings in which the rock surrounding the excavations is always subject to high compressive stresses, it may be reasonable to treat a jointed rock mass as an equivalent elastic continuum. A simple example of the way in which rock material and discontinuity properties may be combined to obtain the elastic properties of the equivalent continuum is given in section 4.9.2.

Figure 4.1 illustrates the transition from intact rock to a heavily jointed rock mass with increasing sample size in a hypothetical rock mass surrounding an underground excavation. Which model will apply in a given case will depend on the size of the excavation relative to the discontinuity spacing, the imposed stress level, and the orientations and strengths of the discontinuities. Those aspects of the stress–strain behaviour of rocks and rock masses required to solve these various classes of problem, will be discussed in this chapter. Since compressive stresses predominate in geotechnical problems, the emphasis will be on response to compressive and shear stresses. For the reasons outlined in section 1.2.3, the response to tensile stresses will not be considered in detail.

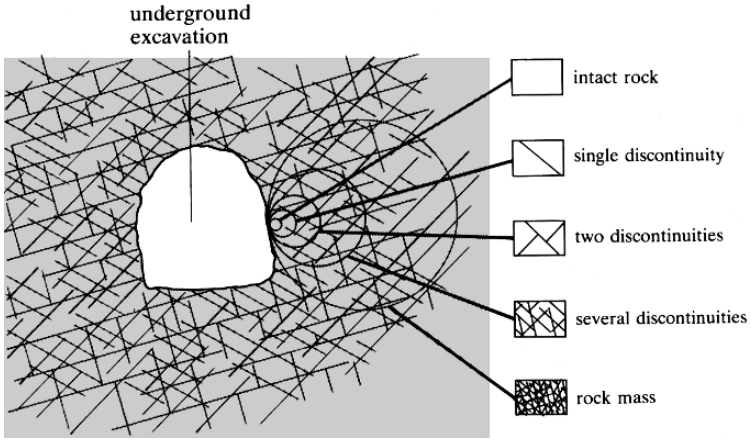


**Figure 4.1** Idealised illustration of the transition from intact rock to a heavily jointed rock mass with increasing sample size (after Hoek and Brown, 1980).

## 4.2 Concepts and definitions

Experience has shown that the terminology used in discussions of rock 'strength' and 'failure' can cause confusion. Unfortunately, terms which have precise meanings in engineering science are often used imprecisely in engineering practice. In this text, the following terminology and meanings will be used.

**Fracture** is the formation of planes of separation in the rock material. It involves the breaking of bonds to form new surfaces. The onset of fracture is not necessarily synonymous with failure or with the attainment of peak strength.

**Strength**, or **peak strength**, is the maximum stress, usually averaged over a plane, that the rock can sustain under a given set of conditions. It corresponds to point B in Figure 4.2a. After its peak strength has been exceeded, the specimen may still have some load-carrying capacity or strength. The minimum or **residual strength** is reached generally only after considerable post-peak deformation (point C in Figure 4.2a).

**Brittle fracture** is the process by which sudden loss of strength occurs across a plane following little or no permanent (plastic) deformation. It is usually associated with strain-softening or strain-weakening behaviour of the specimen as illustrated in Figure 4.2a.

**Ductile deformation** occurs when the rock can sustain further permanent deformation without losing load-carrying capacity (Figure 4.2b).

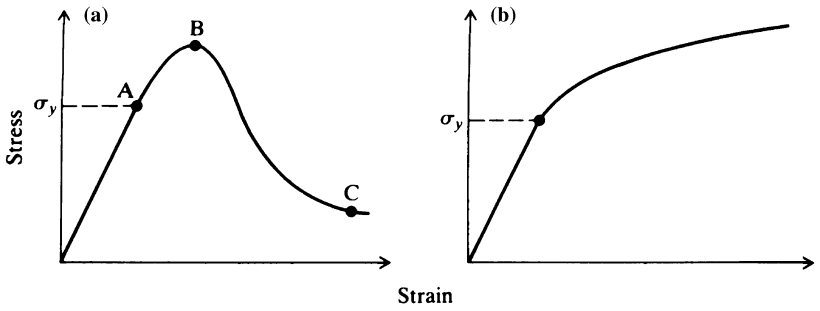


**Figure 4.2** (a) Strain-softening; (b) strain-hardening stress–strain curves.

**Yield** occurs when there is a departure from elastic behaviour, i.e. when some of the deformation becomes irrecoverable as at A in Figure 4.2a. The **yield stress** ($\sigma_y$ in Figure 4.2) is the stress at which permanent deformation first appears.

**Failure** is often said to occur at the peak strength or be initiated at the peak strength (Jaeger and Cook, 1979). An alternative engineering approach is to say that the rock has failed when it can no longer adequately support the forces applied to it or otherwise fulfil its engineering function. This may involve considerations of factors other than peak strength. In some cases, excessive deformation may be a more appropriate criterion of 'failure' in this sense.

**Effective stress** is defined, in general terms, as the stress which governs the gross mechanical response of a porous material. The effective stress is a function of the total or applied stress and the pressure of the fluid in the pores of the material, known as the **pore pressure** or **pore-water pressure.** The concept of effective stress was first developed by Karl Terzaghi who used it to provide a rational basis for the understanding of the engineering behaviour of soils. Terzaghi's formulation of the **law of effective stress**, an account of which is given by Skempton (1960), is probably the single most important contribution ever made to the development of geotechnical engineering. For soils and some rocks loaded under particular conditions, the effective stresses, $\sigma'_{ij}$, are given by

$$\sigma'_{ij} = \sigma_{ij} - u\delta_{ij} \tag{4.1}$$

where $\sigma_{ij}$ are the total stresses, $u$ is the pore pressure, and $\delta_{ij}$ is the Kronecker delta. This result is so well established for soils that it is often taken to be the definition of effective stress. Experimental evidence and theoretical argument suggest that, over a wide range of material properties and test conditions, the response of rock depends on

$$\sigma'_{ij} = \sigma_{ij} - \alpha u\delta_{ij} \tag{4.2}$$

where $\alpha \leqslant 1$, and is a constant for a given case (Paterson, 1978).

## 4.3 Behaviour of isotropic rock material in uniaxial compression

### *4.3.1 Influence of rock type and condition*

Uniaxial compression of cylindrical specimens prepared from drill core, is probably the most widely performed test on rock. It is used to determine the uniaxial or unconfined compressive strength, $\sigma_c$, and the elastic constants, Young's modulus, $E$, and Poisson's ratio, $\nu$, of the rock material. The uniaxial compressive strength of the intact rock is used in rock mass classification schemes (section 3.7), and as a basic parameter in the rock mass strength criterion to be introduced later in this chapter.

Despite its apparent simplicity, great care must be exercised in interpreting results obtained in the test. Obviously, the observed response will depend on the nature and composition of the rock and on the condition of the test specimens. For similar mineralogy, $\sigma_c$ will decrease with increasing porosity, increasing degree of weathering and increasing degree of microfissuring. As noted in section 1.2.4, $\sigma_c$ may also decrease

with increasing water content. Data illustrating these various effects are presented by Vutukuri *et al*. (1974).

It must be recognised that, because of these effects, the uniaxial compressive strengths of samples of rock having the same geological name, can vary widely. Thus the uniaxial compressive strength of sandstone will vary with the grain size, the packing density, the nature and extent of cementing between the grains, and the levels of pressure and temperature that the rock has been subjected to throughout its history. However, the geological name of the rock type can give some qualitative indication of its mechanical behaviour. For example, a slate can be expected to exhibit cleavage which will produce anisotropic behaviour, and a quartzite will generally be a strong, brittle rock. Despite the fact that such features are typical of some rock types, it is dangerous to attempt to assign mechanical properties to rock from a particular location on the basis of its geological description alone. There is no substitute for a well-planned and executed programme of testing.

### *4.3.2 Standard test procedure and interpretation*

Suggested techniques for determining the uniaxial compressive strength and deformability of rock material are given by the International Society for Rock Mechanics Commission on Standardization of Laboratory and Field Tests (ISRM Commission, 1979). The essential features of the recommended procedure are:

(a) The test specimens should be right circular cylinders having a height to diameter ratio of 2.5–3.0 and a diameter preferably of not less than NX core size, approximately 54 mm. The specimen diameter should be at least 10 times the size of the largest grain in the rock.
(b) The ends of the specimen should be flat to within 0.02 mm and should not depart from perpendicularity to the axis of the specimen by more than 0.001 rad or 0.05 mm in 50 mm.
(c) The use of capping materials or end surface treatments other than machining is not permitted.
(d) Specimens should be stored, for no longer than 30 days, in such a way as to preserve the natural water content, as far as possible, and tested in that condition.
(e) Load should be applied to the specimen at a constant stress rate of 0.5–1.0 MPa $s^{-1}$.
(f) Axial load and axial and radial or circumferential strains or deformations should be recorded throughout each test.
(g) There should be at least five replications of each test.

Figure 4.3 shows an example of the results obtained in such a test. The axial force recorded throughout the test has been divided by the initial cross-sectional area of the specimen to give the average axial stress, $\sigma_a$, which is shown plotted against overall axial strain, $\varepsilon_a$, and against radial strain, $\varepsilon_r$. Where post-peak deformations are recorded (section 4.3.7), the cross-sectional area may change considerably as the specimen progressively breaks up. In this case, it is preferable to present the experimental data as force–displacement curves.

In terms of progressive fracture development and the accumulation of deformation, the stress-strain or load-deformation responses of rock material in uniaxial compression generally exhibit the four stages illustrated in Figure 4.3. An initial bedding down and crack closure stage is followed by a stage of elastic deformation until an axial

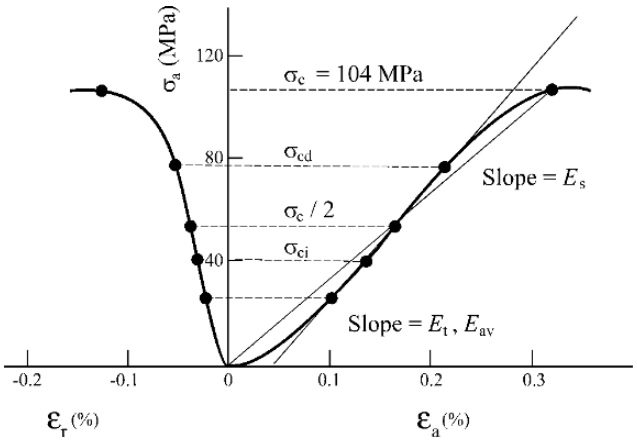


**Figure 4.3** Results obtained in a uniaxial compression test on rock.

stress of $\sigma_{ci}$ is reached at which stable crack propagation is initiated. This continues until the axial stress reaches $\sigma_{cd}$ when unstable crack growth and irrecoverable deformations begin. This region continues until the peak or uniaxial compressive strength, $\sigma_c$, is reached. The processes involved in these stages of loading will be discussed later in this Chapter.

As shown in Figure 4.3, the axial Young's modulus of the specimen varies throughout the loading history and so is not a uniquely determined constant for the material. It may be calculated in a number of ways, the most common being:

(a) **Tangent Young's modulus**, $E_t$, is the slope of the axial stress–axial strain curve at some fixed percentage, generally 50%, of the peak strength. For the example shown in Figure 4.3, $E_t = 51.0$ GPa.
(b) **Average Young's modulus**, $E_{av}$, is the average slope of the more-or-less straight line portion of the axial stress–strain curve. For the example shown in Figure 4.3, $E_{av} = 51.0$ GPa.
(c) **Secant Young's modulus**, $E_s$, is the slope of a straight line joining the origin of the axial stress–strain curve to a point on the curve at some fixed percentage of the peak strength. In Figure 4.3, the secant modulus at peak strength is $E_s = 32.1$ GPa.

Corresponding to any value of Young's modulus, a value of Poisson's ratio may be calculated as

$$\nu = -\frac{(\Delta\sigma_a/\Delta\varepsilon_a)}{(\Delta\sigma_a/\Delta\varepsilon_r)} \tag{4.3}$$

For the data given in Figure 4.3, the values of $\nu$ corresponding to the values of $E_t$, $E_{av}$, and $E_s$ calculated above are approximately 0.29, 0.31 and 0.40 respectively.

Because of the axial symmetry of the specimen, the volumetric strain, $\varepsilon_v$, at any stage of the test can be calculated as

$$\varepsilon_v = \varepsilon_a + 2\varepsilon_r \tag{4.4}$$

For example, at a stress level of $\sigma_a = 80$ MPa in Figure 4.3, $\varepsilon_a = 0.220\%$, $\varepsilon_r = -0.055\%$ and $\varepsilon_v = 0.110\%$.

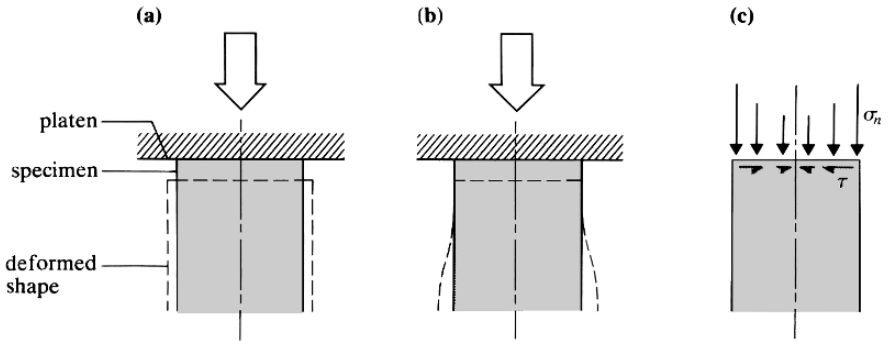


**Figure 4.4** Influence of end restraint on stresses and displacements induced in a uniaxial compression test: (a) desired uniform deformation of the specimen; (b) deformation with complete radial restraint at the specimen–platen contact; (c) non-uniform normal stress, $\sigma_n$ and shear stress, $\tau$ induced at the specimen end as a result of end restraint.

Varying the standard conditions will influence the observed response of the specimen. Some of these effects will be discussed briefly in sections 4.3.3 to 4.3.7. More extensive discussions of these effects are given by Hawkes and Mellor (1970), Vutukuri *et al*. (1974) and Paterson (1978).

### *4.3.3 End effects and the influence of height to diameter ratio*

The objective of the test arrangements should be to subject the specimen to uniform boundary conditions with a uniform uniaxial stress and a uniform displacement field being produced throughout the specimen (Figure 4.4a). Due to friction between the specimen ends and the platens and differences between the elastic properties of rock and steel, the specimen will be restrained near its ends and prevented from deforming uniformly. Figure 4.4b illustrates a case in which complete radial restraint occurs at the specimen ends. The result of such restraint is that shear stresses are set up at the specimen–platen contact (Figure 4.4c). This means that the axial stress is not a principal stress and that the stresses within the specimen are not always uniaxial.

As a consequence of these end effects, the stress distribution varies throughout the specimen as a function of specimen geometry. As the height to diameter ($H/D$) ratio increases, a greater proportion of the sample volume is subjected to an approximately uniform state of uniaxial stress. It is for this essential reason that a $H/D$ ratio of at least 2.0 should be used in laboratory compression testing of rock. Figure 4.5 shows some experimental data which illustrate this effect. When 51 mm diameter specimens of Wombeyan Marble were loaded through 51 mm diameter steel platens, the measured uniaxial compressive strength increased as the $H/D$ ratio was decreased and the shape of the post-peak stress–strain curve became flatter. When the tests were repeated with 'brush' platens (made from an assembly of 3.2 mm square high-tensile steel pins), lateral deformation of the specimens was not inhibited; similar stress–strain curves were obtained for $H/D$ ratios in the range 0.5 to 3.0 However, 'brush' platens were found to be too difficult to prepare and maintain for their use in routine testing to be recommended.

It is tempting to seek to eliminate end effects by treating the specimen–platen interface with a lubricant or by inserting a sheet of soft material between the specimen and the platen. Experience has shown that this can cause lateral tensile stresses to be applied to the specimen by extrusion of the inserts or by fluid pressures set up inside flaws on the specimen ends. For this reason, the ISRM Commission (1979) and other

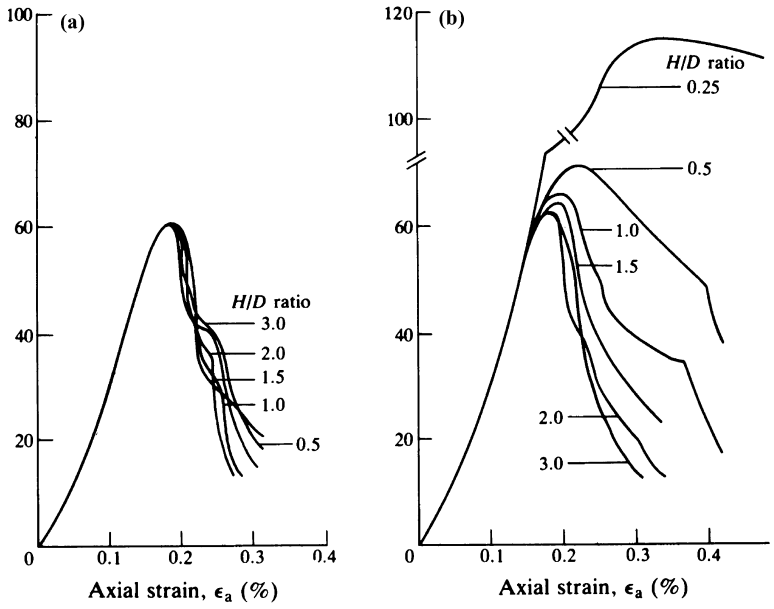


**Figure 4.5** Influence of height to diameter ($H/D$) ratio on stress-strain curves obtained in uniaxial compression tests carried out on Wombeyan Marble using (a) brush platens, and (b) solid steel platens (after Brown and Gonano, 1974).

authorities (e.g. Hawkes and Mellor, 1970; Jaeger and Cook, 1979) recommend that treatment of the sample ends, other than by machining, be avoided.

### *4.3.4 Influence of the standard of end preparation*

In Figures 4.3 and 4.5, the axial stress-axial strain curves have initial concave upwards sections before they become sensibly linear. This initial portion of the curve is generally said to be associated with 'bedding-down' effects. However, experience shows that the extent of this portion of the curve can be greatly reduced by paying careful attention to the flatness and parallelism of the ends of the specimen. Analyses of the various ways in which a poor standard of end preparation influence the observed response of the sample have been presented by Hawkes and Mellor (1970).

The ISRM Commission (1979) recommends that in a 50+ mm diameter specimen, the ends should be flat to within 0.02 mm and should not depart from the perpendicular to the specimen axis by more than 0.05 mm. The latter figure implies that the ends could be out of parallel by up to 0.10 mm. Even when spherical seats are provided in the platens, out-of-parallelism of this order can still have a significant influence on the shape of the stress–strain curve, the peak strength and the reproducibility of results. For research investigations, the authors prepare their 50–55 mm diameter specimens with ends flat and parallel to within 0.01 mm.

### *4.3.5 Influence of specimen volume*

It has often been observed experimentally that, for similar specimen geometry, the uniaxial compressive strength of rock material, $\sigma_c$, varies with specimen volume. (This is a different phenomenon to that discussed in section 4.1 where the changes in behaviour considered were those due to the presence of varying numbers of geological discontinuities within the sample volume.) Generally, it is observed that $\sigma_c$ decreases with increasing specimen volume, except at very small specimen sizes

where inaccuracy in specimen preparation and surface flaws or contamination may dominate behaviour and cause a strength decrease with decreasing specimen volume. This, coupled with the requirement that the specimen diameter should be at least 10 times the size of the largest grain, provides a reason for using specimen diameters of approximately 50 mm in laboratory compression tests.

Many explanations have been offered for the existence of size effects, but none has gained universal acceptance. A popular approach is to interpret size effects in terms of the distribution of flaws within the material. Much of the data on which conclusions about size effects are based, were obtained using cubical specimens. Brown and Gonano (1975) have shown that in these cases, stress gradients and end effects can greatly influence the results obtained. The most satisfactory explanations of observed size effects in rock and other brittle materials are those in which surface energy is used as the fundamental material property (section 4.5.3).

### *4.3.6 Influence of strain rate*

The ISRM Commission (1979) recommends that a loading rate of 0.5–1.0 MPa $s^{-1}$ be used in uniaxial compression tests. This corresponds to a time to the attainment of peak strength in the order of 5–10 min. As the arguments presented below show, it is preferable to regard strain or deformation, rather than axial stress or load, as the controlling variable in the compression testing of rock. For this reason, the following discussion will be in terms of axial strain rate, $\dot{\varepsilon}_a$, rather than axial stress rate.

The times to peak strength recommended by the ISRM Commission (1979) correspond to axial strain rates in the order of $10^{-5}$–$10^{-4}$ $s^{-1}$. For rocks other than those such as the evaporites which exhibit markedly time-dependent behaviour, departures from the prescribed strain rate by one or two orders of magnitude may produce little discernible effect. For very fast and very slow strain rates, differences in the observed stress–strain behaviour and peak strengths can become quite marked. However, a change in strain rate from $10^{-8}$ $s^{-1}$ to $10^{2}$ $s^{-1}$ may only increase the measured uniaxial compressive strength by a factor of about two. Generally, the observed behaviour of rock is not significantly influenced by varying the strain rate within the range that it is convenient to use in quasi-static laboratory compression tests.

### *4.3.7 Influence of testing machine stiffness*

Whether or not the post-peak portion of the stress–strain curve can be followed and the associated progressive disintegration of the rock studied, depends on the relative stiffnesses of the specimen and the testing machine. The standard test procedure and interpretation discussed in section 4.3.2 do not consider this post-peak behaviour. However, the subject is important in assessing the likely stability of rock fracture in mining applications including pillar stability and rockburst potential.

Figure 4.6 illustrates the interaction between a specimen and a conventional testing machine. The specimen and machine are regarded as springs loaded in parallel. The machine is represented by a linear elastic spring of constant longitudinal stiffness, $k_m$, and the specimen by a non-linear spring of varying stiffness, $k_s$. Compressive forces and displacements of the specimen are taken as positive. Thus as the specimen is compressed, the machine spring extends. (This extension is analogous to that which occurs in the columns of a testing machine during a compression test.) When the peak strength has been reached in a strain-softening specimen such as that shown

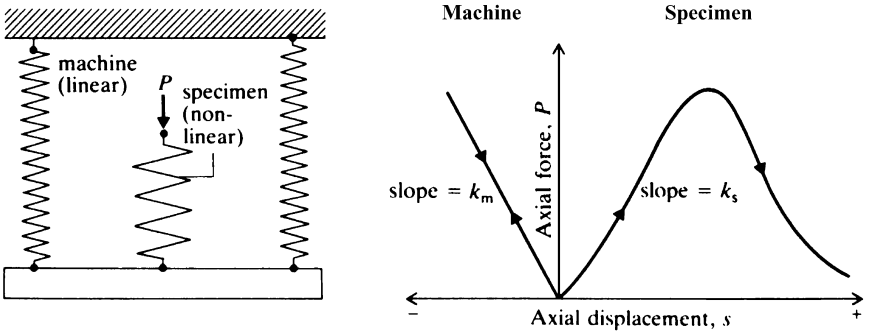


**Figure 4.6** Spring analogy illustrating machine–specimen interaction.

in Figure 4.6, the specimen continues to compress, but the load that it can carry progressively reduces. Accordingly, the machine unloads and its extension reduces.

Figure 4.7 shows what will happen if the machine is (a) soft, and (b) stiff, with respect to the specimen. Imagine that the specimen is at peak strength and is compressed by a small amount, $\Delta$s. In order to accommodate this displacement, the load on the specimen must reduce from $P_A$ to $P_B$, so that an amount of energy $\Delta W_s$, given by the area ABED in Figures 4.7 a and b, is absorbed. However, in displacing by $\Delta$s from point A, the 'soft' machine only unloads to F and releases stored strain energy $\Delta W_m$, given by the area AFED. In this case $\Delta W_m > \Delta W_s$, and catastrophic failure occurs at, or shortly after, the peak because the energy released by the machine during unloading is greater than that which can be absorbed by the specimen in following the post-peak curve from A to B.

If the machine is stiff with respect to the specimen in the post-peak region, the post-peak curve can be followed. In Figure 4.7b, $\Delta W_m < \Delta W_s$ and energy in excess of that released by the machine as stored strain energy must be supplied in order to deform the specimen along ABC. Note that the behaviour observed up to, and including, the peak, is not influenced by machine stiffness.

For some very brittle rocks, generally those that are fine grained and homogeneous, portions of the post-peak force–displacement or stress–strain curves can be very steep so that it becomes impossible to 'control' post-peak deformation even in the stiffest of testing machines. In these cases, the post-peak curves and the associated mechanisms of fracture may be studied using a judiciously operated **servocontrolled testing machine**.

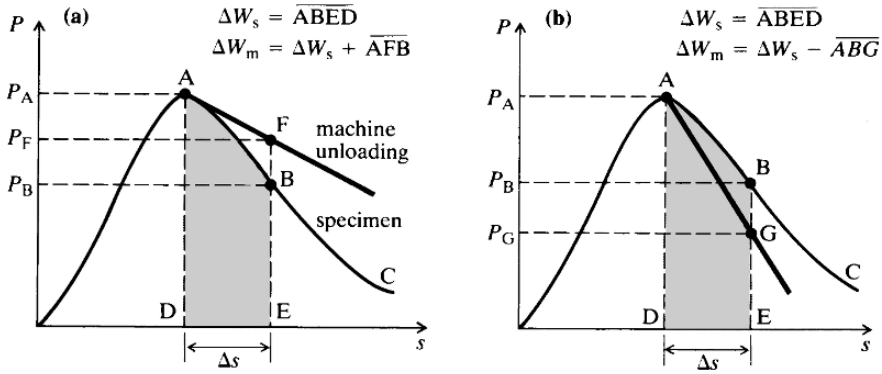


**Figure 4.7** Post-peak unloading using machines that are (a) soft, and (b) stiff, with respect to the specimen.

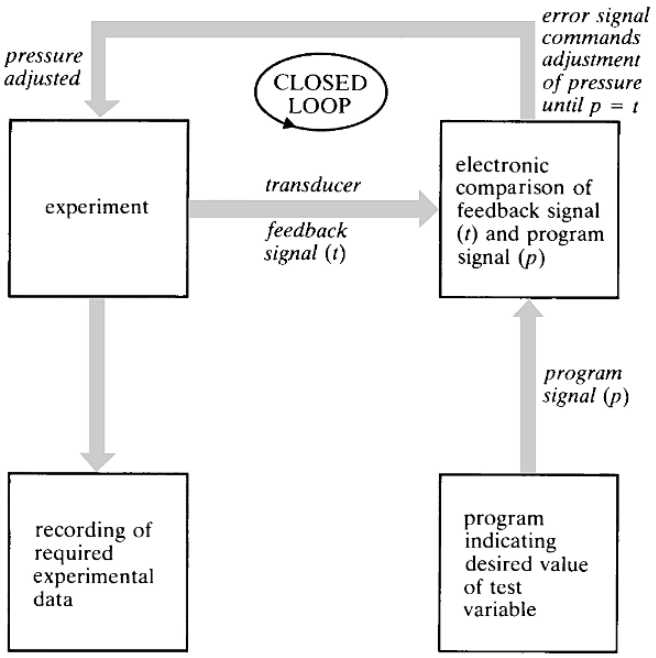


**Figure 4.8** Principle of closed-loop control (after Hudson *et al.,* 1972b).

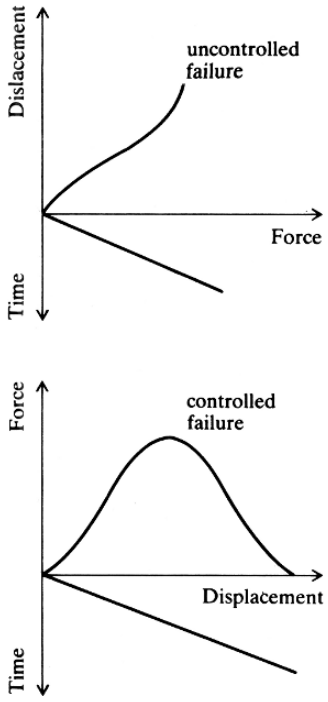


**Figure 4.9** Choice between force and displacement as the programmed control variable (after Hudson *et al.*, 1972a).

The essential features of closed-loop servocontrol are illustrated in Figure 4.8. An experimental variable (a force, pressure, displacement or strain component) is programmed to vary in a predetermined manner, generally monotonically increasing with time. The measured and programmed values are compared electronically several thousands of times a second, and a servo valve adjusts the pressure within the actuator to produce the desired equivalence.

Modern servocontrolled testing systems are used to conduct a wide variety of tests in rock mechanics laboratories. The key to the successful use of these systems is the choice of the control variable. The basic choice is between a force (or pressure) and a displacement (or strain) component. Figure 4.9 shows why it is not feasible to obtain the complete uniaxial force–displacement curve for a strain-softening specimen by programming the axial force to increase monotonically with time. When the peak strength of the specimen is reached, the program will attempt to continue to increase the axial force, but the load-carrying capacity can only decrease with further axial displacement. However, the test can be successfully controlled by programming the axial **displacement** to increase monotonically with time.

The post-peak portions of the force–displacement curves obtained in compression tests on some rocks may be steeper than, or not as smooth as, those shown in Figures 4.7 and 4.9. In these cases, better control can be obtained by using the circumferential displacement rather than the axial displacement as the control variable. Figure 4.10 shows the complete axial stress ($\sigma_a$)–axial strain ($\varepsilon_a$) and circumferential (or radial) strain ($\varepsilon_r$)–axial strain curves obtained in such a test on a 50 mm diameter by 100 mm long specimen of an oolitic limestone (Portland stone) in which a wrap-around transducer was used to monitor circumferential displacement. Although the possibility of extracting energy from the machine–specimen system offered by this technique is

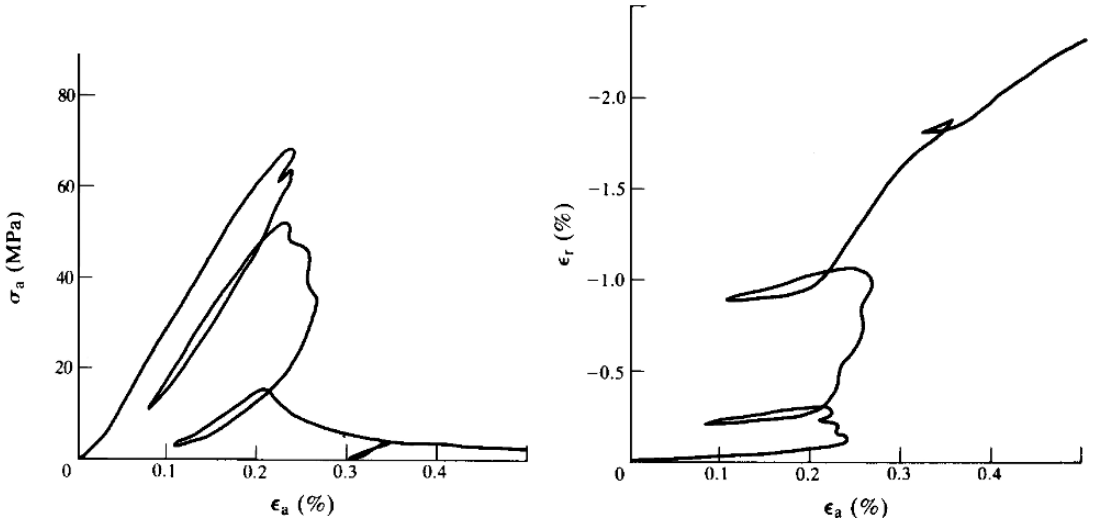


**Figure 4.10** Axial stress, $\sigma_a$, and radial strain, $\varepsilon_r$, vs. axial strain, $\varepsilon_a$, curves recorded in a uniaxial compression test on an oolitic limestone (after Elliott, 1982).

not reproduced in practical mining problems, this approach does permit progressive post-peak breakdown to be controlled and studied.

Figure 4.11 shows the complete $\sigma_a$–$\varepsilon_a$ curves obtained by Wawersik and Fairhurst (1970) in a series of controlled uniaxial compression tests on a range of rock types. By halting tests on specimens of the same rock at different points on the curve and sectioning and polishing the specimens, Wawersik and Fairhurst were able to study the mechanisms of fracture occurring in the different rock types. They found that the post-peak behaviours of the rocks studied may be divided into two classes

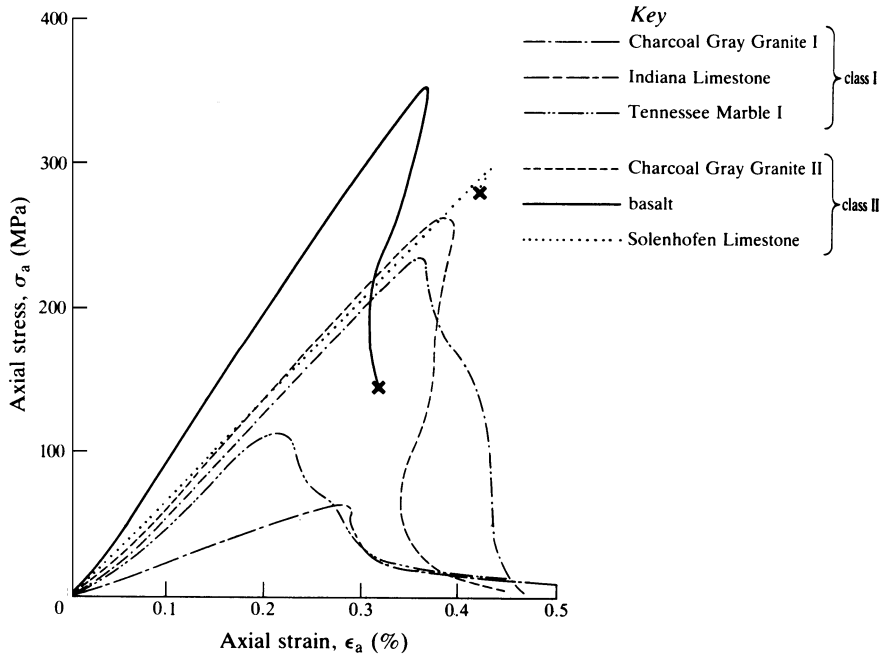


**Figure 4.11** Uniaxial stress–strain curves for six rocks (after Wawersik and Fairhurst, 1970).

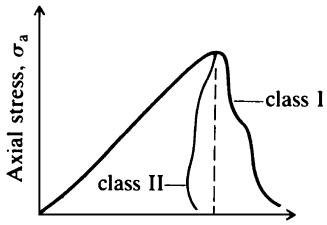


**Figure 4.12** Two classes of stress–strain behavior observed in uniaxial compression tests (after Wawersik and Fairhurst, 1970).

(Figure 4.12). For class I behaviour, fracture propagation is stable in the sense that work must be done on the specimen for each incremental decrease in load-carrying ability. For class II behaviour, the fracture process is unstable or self-sustaining; to control fracture, energy must be extracted from the material.

The experiments of Wawersik and Fairhurst and of subsequent investigators, indicate that, in uniaxial compression, two different modes of fracture may occur:

(a) local 'tensile' fracture predominantly parallel to the applied stress;
(b) local and macroscopic shear fracture (faulting).

The relative predominance of these two types of fracture depends on the strength, anisotropy, brittleness and grain size of the crystalline aggregates. However, sub-axial fracturing generally precedes faulting, being initiated at 50–95% of the peak strength.

In very heterogeneous rocks, sub-axial fracturing is often the only fracture mechanism associated with the peaks of the $\sigma_a$–$\varepsilon_a$ curves for both class I and class II behaviour. In such rocks, shear fractures develop at the boundaries and then in the interiors of specimens, well beyond the peak. This observation is at variance with the traditional view that through-going shear fracture occurs *at* the peak. Generally, these shear fractures, observed in 'uncontrolled' tests, are associated with sudden unloading in a soft testing machine.

In homogeneous, fine-grained rocks such as the Solenhofen Limestone (Figure 4.11), the peak compressive strength may be governed by localised faulting. Because of the internal structural and mechanical homogeneity of these rocks, there is an absence of the local stress concentrations that may produce pre-peak cracking throughout coarser-grained crystalline aggregates. In these homogeneous, fine-grained rocks, fracture initiation and propagation can occur almost simultaneously. If violent post-peak failure of the specimen is to be prevented, the strain energy stored in the unfractured parts of the specimen, and in the testing machine, must be removed rapidly by reversing the sense of platen movement. This produces the artefact of a class II curve.

It is important to recognise that the post-peak portion of the curve does not reflect a true material property. The appearance of localised faulting in laboratory tests on rock and around underground excavations may be explained at a fundamental level by bifurcation or strain localisation analysis. In this approach, it is postulated that the material properties may allow the homogeneous deformation of an initially uniform material to lead to a bifurcation point, at which non-uniform deformation can be incipient in a planar band under conditions of continuing equilibrium and continuing homogeneous deformation outside the zone of localisation (Rudnicki and Rice, 1975). Using a rigorous analysis of this type with the required material properties determined from measured stress–strain and volumetric strain curves, Vardoulakis *et al*. (1988) correctly predicted the axial stress at which a particular limestone failed by faulting in a uniaxial compression test, the orientation of the faults and the Coulomb shear strength parameters (section 4.5.2) of the rock.

### *4.3.8 Influence of loading and unloading cycles*

Figure 4.13 shows the axial force–axial displacement curve obtained by Wawersik and Fairhurst (1970) for a 51 mm diameter by 102 mm long specimen of Tennessee

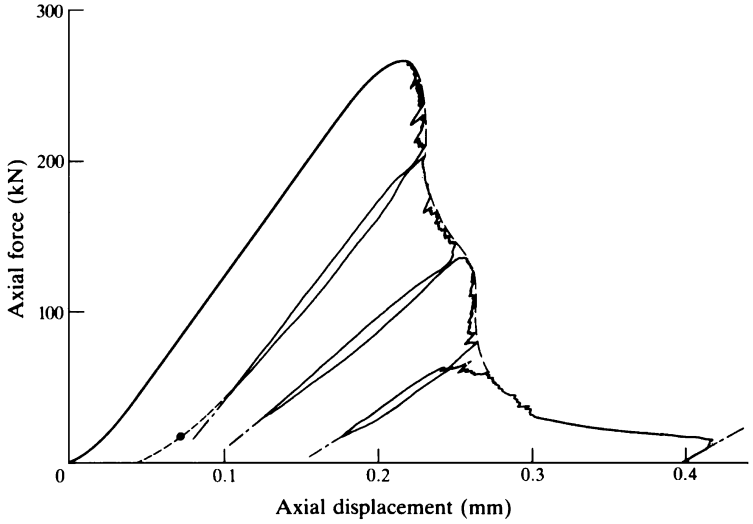


**Figure 4.13** Axial force–axial displacement curve obtained for Tennessee Marble with post-peak unloading and reloading (after Wawersik and Fairhurst, 1970).

Marble which was unloaded and then reloaded from a number of points in the post-peak range. Several points should be noted about the behaviour observed.

(a) On reloading, the curve eventually joins that for a specimen in which the axial displacement increases monotonically with time.
(b) As displacement continues in the post-peak region, the proportion of the total displacement that is irrecoverable increases.
(c) The unloading–loading loop shows some hysteresis.
(d) The apparent modulus of the rock which can be calculated from the slope of the reloading curve, decreases with post-peak deformation and progressive fragmentation of the specimen.

If rock specimens are subjected to loading and unloading cycles in the pre-peak range, some permanent deformation and hysteresis are generally observed. This is often associated with 'bedding-down' effects, and for this reason, the ISRM Commission (1979) recommends that 'it is sometimes advisable for a few cycles of loading and unloading to be performed'.

### *4.3.9 The point load test*

Sometimes the facilities required to prepare specimens and carry out uniaxial compression tests to the standard described above are not available. In other cases, the number of tests required to determine the properties of the range of rock types encountered on a project may become prohibitive. There may be still further cases, in which the uniaxial compressive strength and the associated stress–strain behaviour need not be studied in detail, with only an approximate measure of peak strength being required. In all of these instances, the point load test may be used to provide an indirect estimate of uniaxial compressive strength. This account is based on the ISRM Suggested Method for determining point load strength (ISRM Commission, 1985).

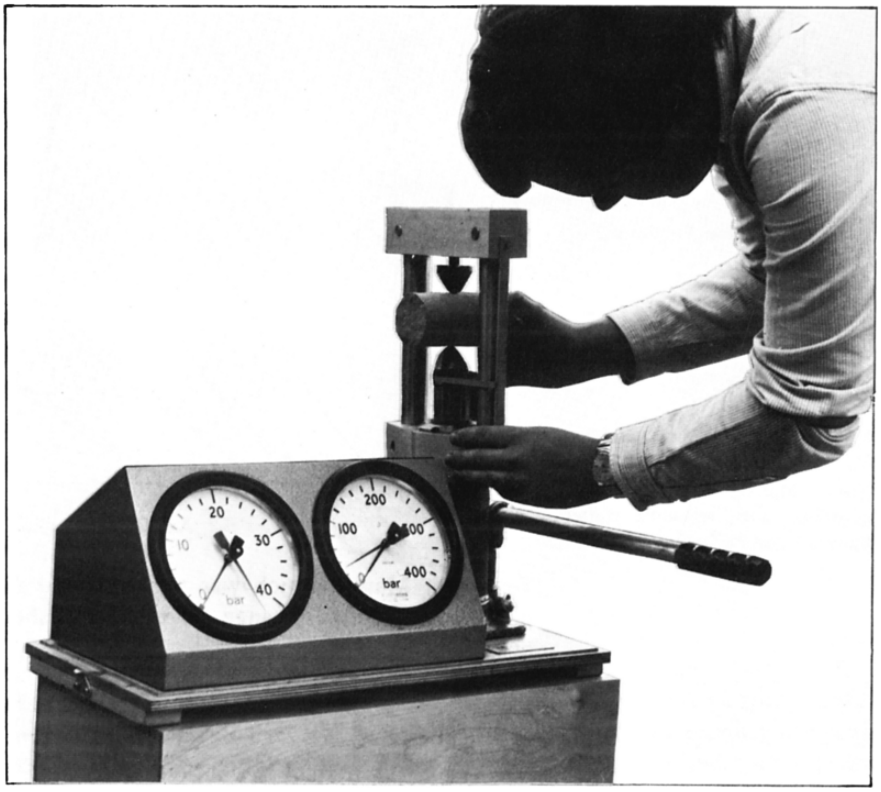


**Figure 4.14** Point load test apparatus (photograph by ELE International Ltd).

In this test, rock specimens in the form of core (the **diametral** and **axial** tests), cut blocks (the **block** test) or irregular lumps (the **irregular lump** test) are broken by a concentrated load applied through a pair of spherically truncated, conical platens. The test can be performed in the field with portable equipment or in the laboratory using apparatus such as that shown in Figure 4.14. The load should be applied at least 0.5D from the ends of the specimen in diametral tests, where $D$ is the core diameter, and equivalent distances in other tests as specified by the ISRM Commission (1985). From the measured value of the force, $P$, at which the test specimen breaks, an **Uncorrected Point Load Index**, $I_s$, is calculated as

$$I_s = \frac{P}{D_e^2} \tag{4.5}$$

where $D_e$, the equivalent core diameter, is given by the core diameter, $D$, for diametral tests, and by $4A/\pi$ for axial, block and lump tests, where $A$ is the minimum cross sectional area of a plane through the specimen and the platen contact points.

The index, $I_s$, varies with $D_e$ and so size correction must be applied in order to obtain a unique point load strength index for a particular rock sample for use for strength classification. Wherever possible, it is preferable to carry out diametral tests on 50–55 mm diameter specimens. The size-corrected **Point Load Strength Index,** $I_{s(50)}$, is defined as the value of $I_s$ that would have been measured in a diametral test with $D = 50$ mm. The results of several series of tests carried out by a number of

investigators show that the value of $I_s$ determined in a test of equivalent diameter, $D_e$, may be converted to an $I_{s(50)}$ value by the relation

$$I_{s(50)} = I_s \times \left(\frac{D_e}{50}\right)^{0.45} \tag{4.6}$$

Beginning with Broch and Franklin (1972), a number of investigators have developed correlations of the Point Load Index with the uniaxial compressive strength, $\sigma_c$. The most commonly used correlation is

$$\sigma_c \approx (22 - 24) I_{s(50)} \tag{4.7}$$

Caution must be exercised in carrying out point load tests and in interpreting the results, especially when correlations such as that given by equation 4.7 are used. The test is one in which fracture is caused by induced tension, and it is essential that a consistent mode of failure be produced if the results obtained from different specimens are to be comparable. Very soft rocks, and highly anisotropic rocks or rocks containing marked planes of weakness such as bedding planes, are likely to give spurious results. A high degree of scatter is a general feature of point load test results and large numbers of individual determinations (often in excess of 100) are required in order to obtain reliable indices. For anisotropic rocks, it is usual to determine a **Strength Anisotropy Index**, $I_{a(50)}$, defined as the ratio of mean $I_{s(50)}$ values measured perpendicular and parallel to the planes of weakness.

## 4.4 Behaviour of isotropic rock material in multiaxial compression

### *4.4.1 Types of multiaxial compression test*

A basic principle of the laboratory testing of rock to obtain data for use in design analyses, is that the boundary conditions applied to the test specimen should simulate those imposed on the rock element *in situ*. This can rarely be achieved. General practice is to study the behaviour of the rock under known uniform applied stress systems.

As was shown in Chapter 2, a general state of three-dimensional stress at a point can be represented by three principal stresses, $\sigma_1$, $\sigma_2$ and $\sigma_3$, acting on mutually orthogonal planes. No shear stresses act on these planes. A plane of particular interest is the boundary of an underground excavation which is a principal plane except in the unusual case in which a shear stress is applied to the boundary surface by the support. The rock surrounding an underground excavation is rarely in a state of uniaxial compression. In the general case, away from the excavation boundary or on the boundary when a normal support stress, $\sigma_3$, is applied, there will be a state of **polyaxial** stress ($\sigma_1 \neq \sigma_2 \neq \sigma_3$). The special case in which $\sigma_2 = \sigma_3$ is called **triaxial** stress. It is this form of multiaxial stress that is most commonly used in laboratory testing. On the boundary of an unsupported excavation, $\sigma_3 = 0$, and a state of **biaxial** stress exists. The behaviour of intact, isotropic rock materials under each of these applied stress conditions will be discussed briefly in the following sections.

### *4.4.2 Biaxial compression* ($\sigma_1 \geqslant \sigma_2, \sigma_3 = 0$)

Biaxial compression tests are carried out by applying different normal stresses to two pairs of faces of a cube, plate or rectangular prism of rock. The great difficulty with such tests is that the end effects described in section 4.3.3 exert an even greater influence on the stress distribution within the specimen than in the case of uniaxial compression. For this reason, fluid rather than solid medium loading is preferred. An alternative approach is to generate a biaxial state of stress at the inner surface of a hollow cylinder by loading it axially with a fluid pressure applied to its outer surface (Hoskins, 1969, Jaeger and Cook, 1979) in a triaxial cell (section 4.4.3). However, in this case, the stresses at 'failure' cannot be measured, but must be calculated using the theory of elasticity which may not be applicable at peak stress. The inner boundary of the hollow cylinder is a zone of high stress gradient which could influence the result. For these reasons, it is recommended that the use of hollow cylinder tests be restricted to the simulation of particular rock mechanics problems such as the behaviour of rock around a shaft, bored raise or borehole.

Brown (1974) carried out a series of biaxial compression tests on 76 mm square by 25 mm thick plates of Wombeyan Marble which were loaded on their smaller faces through (a) 76 mm × 25 mm solid steel platens, and (b) brush platens made from 3.2 mm square steel pins. Figure 4.15 shows the peak strength envelopes obtained in tests carried out at constant $\sigma_2/\sigma_1$ ratios. The data are normalised with respect to the uniaxial compressive strength of the plates, $\sigma_c = 66$ MPa. The increase in peak strength over $\sigma_c$, associated with a given value of $\sigma_2$, was greater for the solid platens than for the brush platens. This was attributed to the influence of end effects. When the brush platens were used, the maximum measured increase in peak strength over

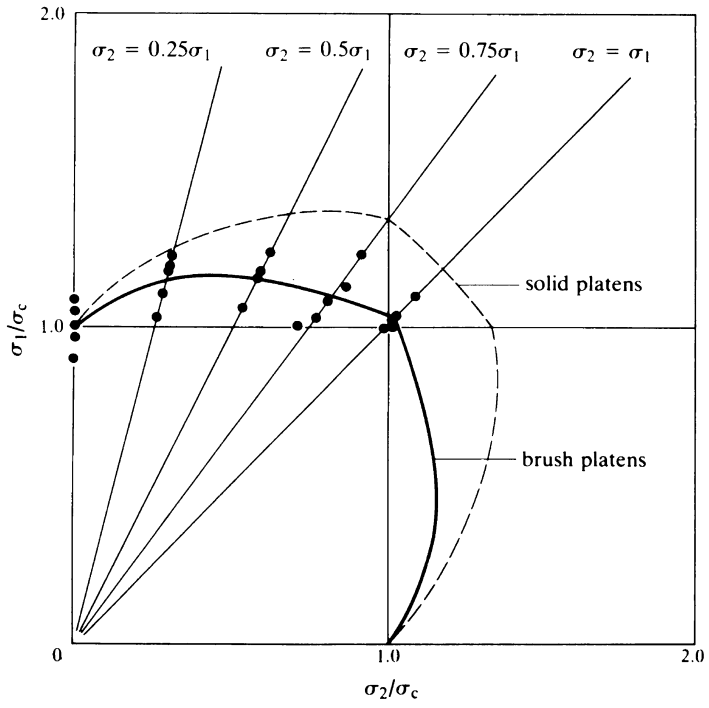


**Figure 4.15** Biaxial compression test results for Wombeyan Marble (after Brown, 1974).

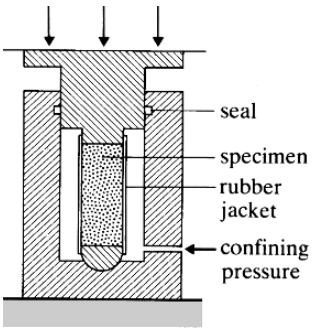


**Figure 4.16** Elements of a conventional triaxial testing apparatus.

$\sigma_c$ was only 15%. For $\sigma_2 = \sigma_1$, no strength increase was observed (i.e. $\sigma_1 = \sigma_c$). The practical consequence of these results is that, for this rock type, the 'strengthening' effect of the intermediate principal stress can be neglected so that the uniaxial compressive strength, $\sigma_c$, should be used as the rock material strength whenever $\sigma_3 = 0$. This slightly conservative conclusion is likely to apply to a wide range of rock types.

### *4.4.3 Triaxial compression* ($\sigma_1 > \sigma_2 = \sigma_3$)

This test is carried out on cylindrical specimens prepared in the same manner as those used for uniaxial compression tests. The specimen is placed inside a pressure vessel (Figures 4.16 and 4.17) and a fluid pressure, $\sigma_3$, is applied to its surface. A jacket, usually made of a rubber compound, is used to isolate the specimen from the confining fluid which is usually oil. The axial stress, $\sigma_1$, is applied to the specimen via a ram passing through a bush in the top of the cell and hardened steel end caps. Pore pressure, $u$, may be applied or measured through a duct which generally connects with the specimen through the base of the cell. Axial deformation of the specimen may be most conveniently monitored by linear variable differential transformers (LVDTs) mounted inside or outside the cell, but preferably inside. Local axial and circumferential strains may be measured by electric resistance strain gauges attached to the surface of the specimen (Figure 4.17).

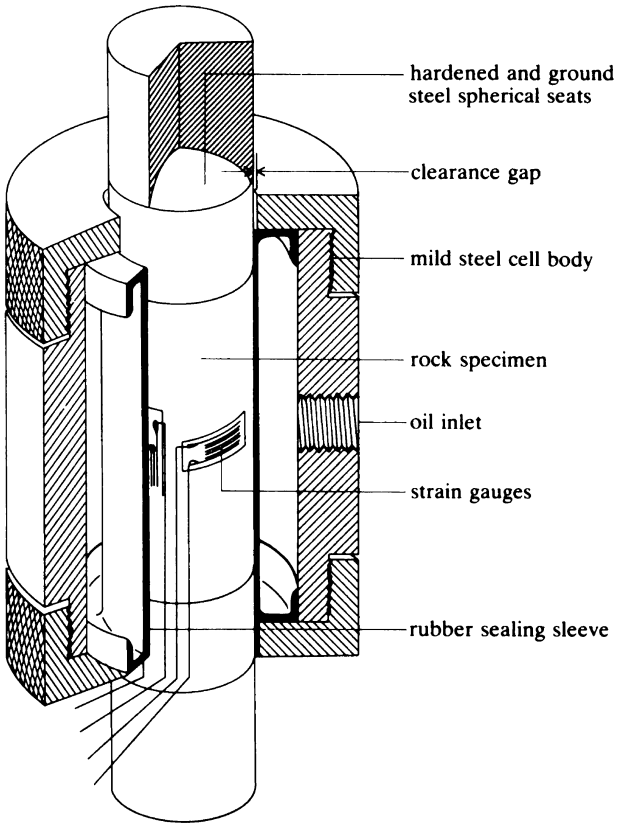


**Figure 4.17** Cut-away view of the triaxial cell designed by Hoek and Franklin (1968). Because this cell does not require drainage between tests, it is well suited to carrying out large numbers of tests quickly.

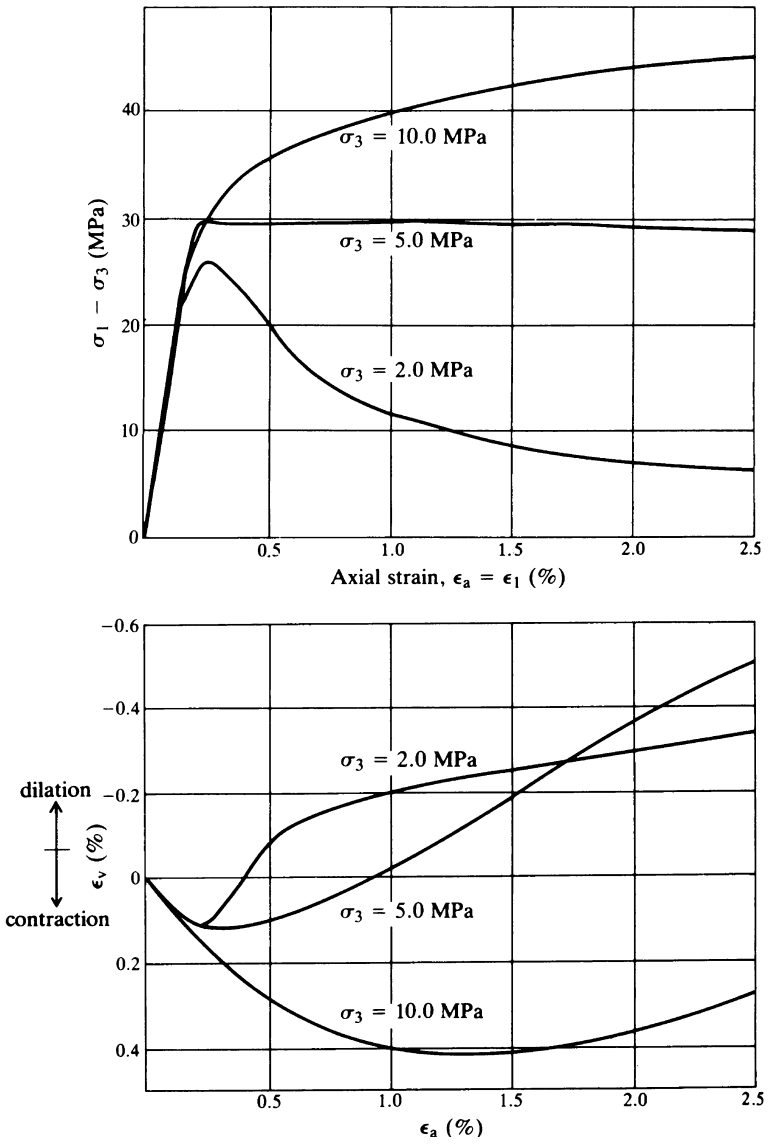


**Figure 4.18** Results of triaxial compression tests on an oolitic limestone with volumetric strain measurement (after Elliott, 1982).

It is necessary to have available for use with the triaxial cell a system for generating the confining pressure and keeping it constant throughout the test. If the confining pressure is generated by a screw-driven pressure intensifier, it is possible to use the displacement of the intensifier plunger to measure the volumetric strain of the specimen (Crouch, 1970). Figure 4.18 shows some results obtained using such a system in tests carried out at three different confining pressures on specimens of an oolitic limestone. An important feature of the behaviour of rock material in triaxial compression is illustrated by Figure 4.18. When the specimen is initially loaded it compresses, but a point is soon reached, generally before the peak of the axial stress–axial strain curve, at which the specimen begins to dilate (increase in volume) as a result of internal fracturing. Shortly after the peak strength is reached, the nett

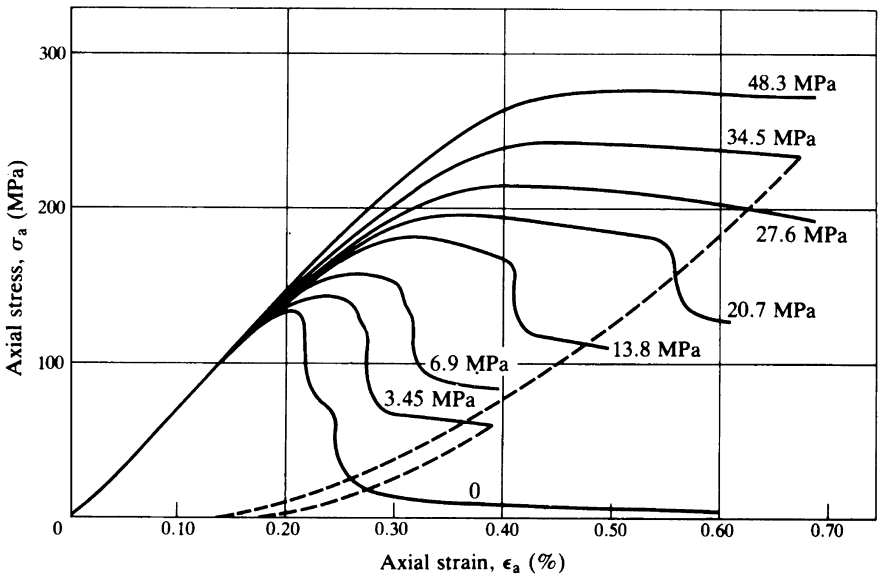


**Figure 4.19** Complete axial stress–axial strain curves obtained in triaxial compression tests on Tennessee Marble at the confining pressures indicated by the numbers on the curves (after Wawersik and Fairhurst, 1970).

volumetric strain of the specimen becomes dilational. Dilation continues in the post-peak range. The amount of dilation decreases with increasing confining pressure. At very high confining pressures, often outside the range of engineering interest, dilation may be totally suppressed with the volumetric strains remaining contractile throughout the test.

Figure 4.19 illustrates a number of other important features of the behaviour of rock in triaxial compression. The axial stress ($\sigma_a$)–axial strain ($\varepsilon_a$) data shown were obtained by Wawersik and Fairhurst (1970) for the Tennessee Marble giving the uniaxial stress–strain curve shown in Figure 4.11. These and similar data for other rocks show that, with increasing confining pressure,

(a) the peak strength increases;
(b) there is a transition from typically brittle to fully ductile behaviour with the introduction of plastic mechanisms of deformation including cataclastic flow and grain-sliding effects;
(c) the region incorporating the peak of the $\sigma_a$–$\varepsilon_a$ curve flattens and widens;
(d) the post-peak drop in stress to the residual strength reduces and disappears at high values of $\sigma_3$.

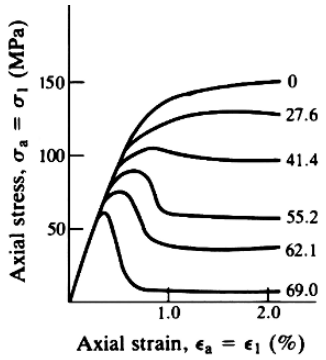


**Figure 4.20** Effect of pore pressure (given in MPa by the numbers on the curves) on the stress–strain behaviour of a limestone tested at a constant confining pressure of 69 MPa (after Robinson, 1959).

The confining pressure at which the post-peak reduction in strength disappears and the behaviour becomes fully ductile ($\sigma_3 = 48.3$ MPa in Figure 4.19), is known as the **brittle–ductile transition pressure** and varies with rock type. In general, the more siliceous igneous and metamorphic rocks such as granite and quartzite remain brittle at room temperature at confining pressures of up to 1000 MPa or more (Paterson, 1978). In these cases, ductile behaviour will not be of concern in practical mining problems.

The influence of pore-water pressure on the behaviour of porous rock in the triaxial compression test is illustrated by Figure 4.20. A series of triaxial compression tests

was carried out on a limestone with a constant value of $\sigma_3 = 69$ MPa, but with various levels of pore pressure in the range $u = 0 - 69$ MPa applied. There is a transition from ductile to brittle behaviour as $u$ is increased from 0 to 69 MPa. In this case, mechanical response is controlled by the effective confining pressure, $\sigma_3' = \sigma_3 - u$, calculated using Terzaghi's classical effective stress law. For less permeable rocks than this limestone, it may appear that the classical effective stress law does not hold. Brace and Martin (1968) conducted triaxial compression tests on a variety of crystalline silicate rocks of low porosity (0.001–0.03) at axial strain rates of $10^{-3}$–$10^{-8}$ $s^{-1}$. They found that the classical effective stress law held only when the strain rate was less than some critical value which depended on the permeability of the rock, the viscosity of the pore fluid and the specimen geometry. At strain rates higher than the critical, static equilibrium could not be achieved throughout the specimen.

### *4.4.4 Polyaxial compression* ($\sigma_1 > \sigma_2 > \sigma_3$)

These tests may be carried out on cubes or rectangular prisms of rock with different normal stresses being applied to each pair of opposite faces. The difficulties caused by end effects are even more marked than in the comparable case of biaxial compression (section 4.4.2). By the addition of an internal fluid pressure, the hollow cylinder biaxial compression test may be converted into a polyaxial test. Hoskins (1969) gives a detailed account of such tests. However, the test also suffers from the difficulties noted for the hollow cylinder biaxial compression test.

The results of polyaxial compression tests on prismatic specimens are often conflicting, but generally indicate some influence of the intermediate principal stress, $\sigma_2$, on stress–strain behaviour. Generally, the peak strength increases with increasing $\sigma_2$ for constant $\sigma_3$, but the effect is not as great as that caused by increasing $\sigma_3$ by a similar amount (Paterson, 1978). However, doubts must remain about the uniformity of the applied stresses in these tests and the results should be interpreted with great care.

### *4.4.5 Influence of stress path*

In the tests described in the preceding sections, it is usual for two of the principal stresses ($\sigma_2$ and $\sigma_3$) to be applied and held constant and for the other principal stress ($\sigma_1$) to be increased towards the peak strength. This stress path is not necessarily that which an element of rock influenced by an excavation will follow when the excavation is made.

As an example, consider a long excavation of circular cross section made in an elastic rock mass in which the *in situ* principal stresses were $p$ vertically, $p$ horizontally parallel to the axis of the excavation, and $0.5p$ horizontally perpendicular to the axis. Results to be presented in Chapter 7 show that on completion of the excavation, the principal stresses at mid-height on the boundary of the excavation change from $\sigma_1 = p$, $\sigma_2 = p$, $\sigma_3 = 0.5p$, to $\sigma_1 = 2.5p$, $\sigma_2 = (1 + \nu)p$ where $\nu$ is Poisson's ratio of the rock, and $\sigma_3 = 0$. As a result of excavation, two principal stresses are increased and the other decreased. It is necessary to determine, therefore, whether the behaviour described earlier is stress-path dependent or whether it is simply a function of the final state of stress.

A test of considerable relevance in this regard is the **triaxial extension test** which is carried out in a triaxial cell with the confining pressure, $\sigma_r$, greater than the axial stress, $\sigma_a$. The test may be commenced at $\sigma_a = \sigma_r$ with $\sigma_a$ being progressively reduced so that

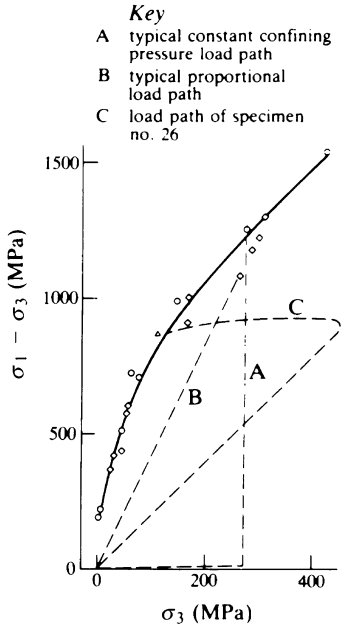


**Figure 4.21** Influence of stress path on the peak strength envelope for Westerly Granite (after Swanson and Brown, 1971).

$\sigma_r = \sigma_1 = \sigma_2 > \sigma_a = \sigma_3$. With modern servocontrolled testing machines, almost any desired total or effective stress path can be followed within the limitations imposed by the axisymmetric configuration of the triaxial cell. Swanson and Brown (1971) investigated the effect of stress path on the peak strength of a granite and a quartz diorite. They found that, for both rock types, the peak strengths in all tests fell on the same envelope (Figure 4.21 for Westerly Granite) irrespective of stress path. They also found that the onset of dilatancy, described in section 4.4.3, is stress-path independent. Similarly, Elliott (1982) found the yield locus of a high-porosity, oolitic limestone to be stress-path independent.

## 4.5 Strength criteria for isotropic rock material

### *4.5.1 Types of strength criterion*

A **peak strength criterion** is a relation between stress components which will permit the peak strengths developed under various stress combinations to be predicted. Similarly, a **residual strength criterion** may be used to predict residual strengths under varying stress conditions. In the same way, a **yield criterion** is a relation between stress components which is satisfied at the onset of permanent deformation. Given that effective stresses control the stress–strain behaviour of rocks, strength and yield criteria are best written in **effective stress** form. However, around most mining excavations, the pore-water pressures will be low, if not zero, and so $\sigma'_{ij} \simeq \sigma_{ij}$. For this reason, it is common in mining rock mechanics to use total stresses in the majority of cases and to use effective stress criteria only in special circumstances.

The data presented in the preceding sections indicate that the general form of the peak strength criterion should be

$$\sigma_1 = f(\sigma_2,\ \sigma_3) \tag{4.8}$$

This is sometimes written in terms of the shear, $\tau$, and normal stresses, $\sigma_n$, on a particular plane in the specimen:

$$\tau = f(\sigma_n) \tag{4.9}$$

Because the available data indicate that the intermediate principal stress, $\sigma_2$, has less influence on peak strength than the minor principal stress, $\sigma_3$, all of the criteria used in practice are reduced to the form

$$\sigma_1 = f(\sigma_3) \tag{4.10}$$

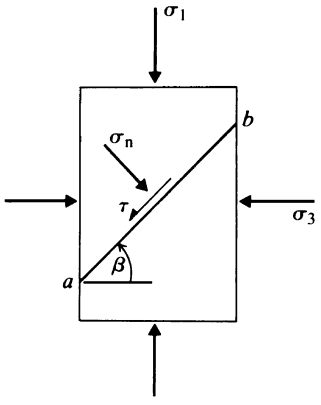


**Figure 4.22** Shear failure on plane *ab*.

### *4.5.2 Coulomb's shear strength criterion*

In one of the classic papers of engineering science, Coulomb (1776) postulated that the shear strengths of rock and of soil are made up of two parts – a constant cohesion and a normal stress-dependent frictional component. (Actually, Coulomb presented his ideas and calculations in terms of forces; the differential concept of stress that we use today was not introduced until the 1820s.) Thus, the shear strength that can be developed on a plane such as *ab* in Figure 4.22 is

$$s = c + \sigma_n \tan\phi \tag{4.11}$$

where $c$ = cohesion and $\phi$ = angle of internal friction.

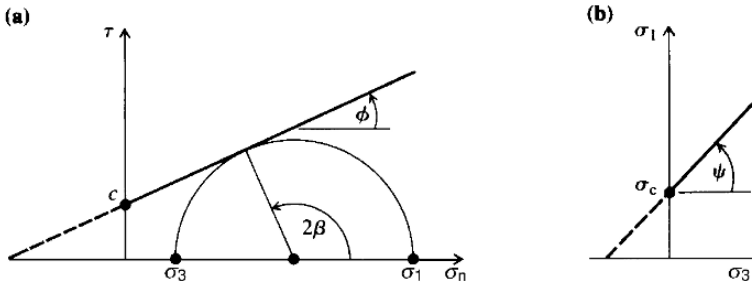


**Figure 4.23** Coulomb strength envelopes in terms of (a) shear and normal stresses, and (b) principal stresses.

Applying the stress transformation equations to the case shown in Figure 4.22 gives

$$\sigma_n = \tfrac{1}{2}(\sigma_1 + \sigma_3) + \tfrac{1}{2}(\sigma_1 - \sigma_3)\cos 2\beta$$

and

$$\tau = \tfrac{1}{2}(\sigma_1 - \sigma_3)\sin 2\beta$$

Substitution for $\sigma_n$ and $s = \tau$ in equation 4.11 and rearranging gives the limiting stress condition on any plane defined by $\beta$ as

$$\sigma_1 = \frac{2c + \sigma_3[\sin 2\beta + \tan\phi\,(1 - \cos 2\beta)]}{\sin 2\beta - \tan\phi\,(1 + \cos 2\beta)} \tag{4.12}$$

There will be a critical plane on which the available shear strength will be first reached as $\sigma_1$ is increased. The Mohr circle construction of Figure 4.23a gives the orientation of this critical plane as

$$\beta = \frac{\pi}{4} + \frac{\phi}{2} \tag{4.13}$$

This result may also be obtained by putting $d(s - \tau)/d\beta = 0$.

For the critical plane, $\sin 2\beta = \cos\phi$, $\cos 2\beta = -\sin\phi$, and equation 4.12 reduces to

$$\sigma_1 = \frac{2c\cos\phi + \sigma_3(1 + \sin\phi)}{1 - \sin\phi} \tag{4.14}$$

This linear relation between $\sigma_3$ and the peak value of $\sigma_1$ is shown in Figure 4.23b. Note that the slope of this envelope is related to $\phi$ by the equation

$$\tan\psi = \frac{1 + \sin\phi}{1 - \sin\phi} \tag{4.15}$$

and that the uniaxial compressive strength is related to $c$ and $\phi$ by

$$\sigma_c = \frac{2c\cos\phi}{1 - \sin\phi} \tag{4.16}$$

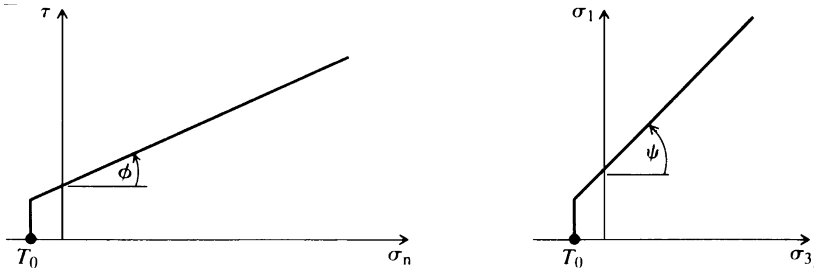


**Figure 4.24** Coulomb strength envelopes with a tensile cut-off.

If the Coulomb envelope shown in Figure 4.23b is extrapolated to $\sigma_1 = 0$, it will intersect the $\sigma_3$ axis at an apparent value of uniaxial tensile strength of the material given by

$$\sigma_T = \frac{2c \cos \phi}{1 + \sin \phi} \tag{4.17}$$

The measurement of the uniaxial tensile strength of rock is fraught with difficulty. However, when it is satisfactorily measured, it takes values that are generally lower than those predicted by equation 4.17. For this reason, a **tensile cutoff** is usually applied at a selected value of uniaxial tensile stress, $T_0$, as shown in Figure 4.24. For practical purposes, it is prudent to put $T_0 = 0$.

Although it is widely used, Coulomb's criterion is not a particularly satisfactory peak strength criterion for rock material. The reasons for this are:

(a) It implies that a major shear fracture exists at peak strength. Observations such as those made by Wawersik and Fairhurst (1970) show that this is not always the case.
(b) It implies a direction of shear failure which does not always agree with experimental observations.
(c) Experimental peak strength envelopes are generally non-linear. They can be considered linear only over limited ranges of $\sigma_n$ or $\sigma_3$.

For these reasons, other peak strength criteria are preferred for intact rock. However, the Coulomb criterion can provide a good representation of residual strength conditions, and more particularly, of the shear strengths of discontinuities in rock (section 4.7).

### *4.5.3 Griffith crack theory*

In another of the classic papers of engineering science, Griffith (1921) postulated that fracture of brittle materials, such as steel and glass, is initiated at tensile stress concentrations at the tips of minute, thin cracks (now referred to as Griffith cracks) distributed throughout an otherwise isotropic, elastic material. Griffith based his determination of the conditions under which a crack would extend on his **energy instability concept**:

> A crack will extend only when the total potential energy of the system of applied forces and material decreases or remains constant with an increase in crack length.

For the case in which the potential energy of the applied forces is taken to be constant throughout, the criterion for crack extension may be written

$$\frac{\partial}{\partial c}(W_d - W_e) \leqslant 0 \tag{4.18}$$

where $c$ is a crack length parameter, $W_e$ is the elastic strain energy stored around the crack and $W_d$ is the surface energy of the crack surfaces.

Griffith (1921) applied this theory to the extension of an elliptical crack of initial length $2c$ that is perpendicular to the direction of loading of a plate of unit thickness subjected to a uniform uniaxial tensile stress, $\sigma$. He found that the crack will extend when

$$\sigma \geqslant \sqrt{\frac{2E\alpha}{\pi c}} \tag{4.19}$$

where $\alpha$ is the surface energy per unit area of the crack surfaces (associated with the rupturing of atomic bonds when the crack is formed), and $E$ is the Young's modulus of the uncracked material.

It is important to note that it is the surface energy, $\alpha$, which is the fundamental material property involved here. Experimental studies show that, for rock, a pre-existing crack does not extend as a single pair of crack surfaces, but a fracture zone containing large numbers of very small cracks develops ahead of the propagating crack (Figure 4.25). In this case, it is preferable to treat $\alpha$ as an **apparent surface energy** to distinguish it from the true surface energy which may have a significantly smaller value.

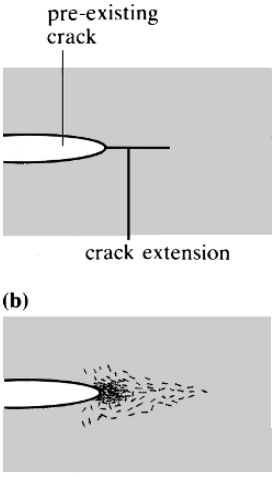


**Figure 4.25** Extension of a preexisting crack, (a) Griffith's hypothesis, (b) the actual case for rock.

It is difficult, if not impossible, to correlate the results of different types of direct and indirect tensile test on rock using the average tensile stress in the fracture zone as the basic material property. For this reason, measurement of the 'tensile strength' of rock has not been discussed in this chapter. However, Hardy (1973) was able to obtain good correlation between the results of a range of tests involving tensile fracture when the apparent surface energy was used as the unifying material property.

Griffith (1924) extended his theory to the case of applied compressive stresses. Neglecting the influence of friction on the cracks which will close under compression, and assuming that the elliptical crack will propagate from the points of maximum tensile stress concentration ($P$ in Figure 4.26), Griffith obtained the following criterion for crack extension in **plane compression**:

$$\begin{aligned} (\sigma_1 - \sigma_2)^2 - 8T_0(\sigma_1 + \sigma_2) = 0 \quad &\text{if } \sigma_1 + 3\sigma_2 > 0 \\ \sigma_2 + T_0 = 0 \quad &\text{if } \sigma_1 + 3\sigma_2 < 0 \end{aligned} \tag{4.20}$$

where $T_0$ is the uniaxial tensile strength of the uncracked material (a positive number).

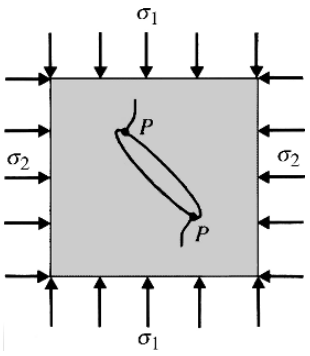


**Figure 4.26** Griffith crack model for plane compression.

This criterion can also be expressed in terms of the shear stress, $\tau$, and the normal stress, $\sigma_n$ acting on the plane containing the major axis of the crack:

$$\tau^2 = 4T_0(\sigma_n + T_0) \tag{4.21}$$

The envelopes given by equations 4.20 and 4.21 are shown in Figure 4.27. Note that this theory predicts that the uniaxial compressive stress at crack extension will always be eight times the uniaxial tensile strength.

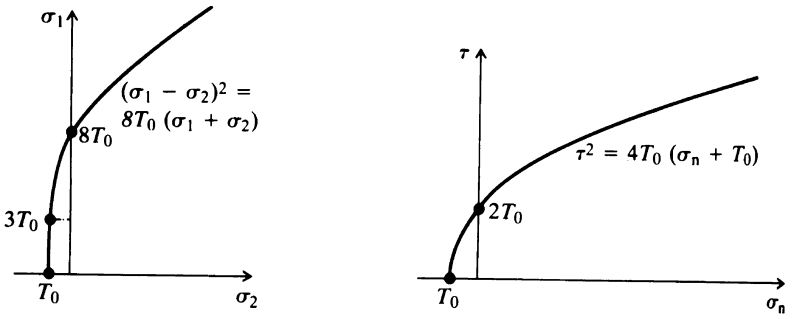


**Figure 4.27** Griffith envelopes for crack extension in plane compression.

During the 1960s, a number of attempts were made to apply these results to the peak strength envelopes for rock. Quite often, $\sigma_2$ in the plane stress criterion was simply replaced by $\sigma_3$ so that the criterion could be applied to triaxial test results. For a number of reasons, the classical Griffith criterion did not provide a very good model for the peak strength of rock under multiaxial compression. Accordingly, a number of modifications to Griffith's solution were introduced (see Paterson, 1978 and Jaeger and Cook, 1979 for details). The most important of these modifications was probably that introduced by Cook (1965) who developed equations for the Griffith locus for instability, or the post-peak stress-strain curve, for rock in compression by assuming shear displacement or sliding on an array of variably inclined cracks.

Using Cook's approach, Martin and Chandler (1994) developed equations for the Griffith locus for rock in triaxial compression which they fitted to triaxial test results obtained for the Lac du Bonnet granite from the Underground Research Laboratory at Pinnawa, Manitoba, Canada. Figure 4.28 shows a comparison of the calculated Griffith locus (solid line) and the measured Griffith locus at confining pressures of 2, 15 and 30 MPa. It was found that as crack-induced damage accumulated in the sample, the stress level associated with crack initiation remained essentially unchanged but that the stress level required to initiate sliding reduced dramatically.

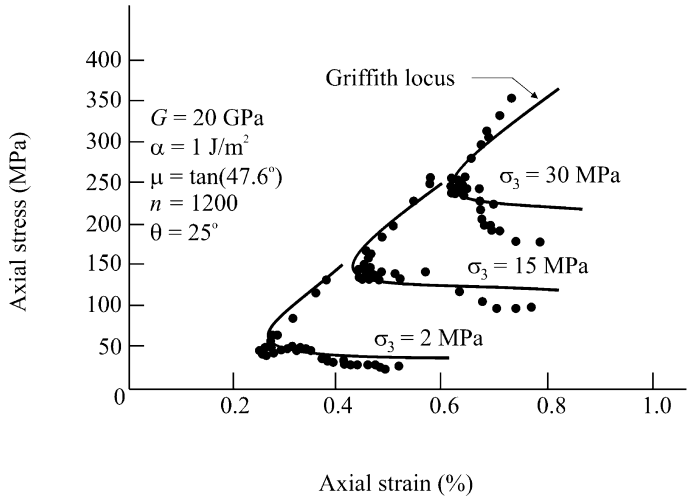


**Figure 4.28** Comparison of calculated Griffith locus (solid line) and measured Griffith locus for Lac du Bonnet granite (after Martin and Chandler, 1994).

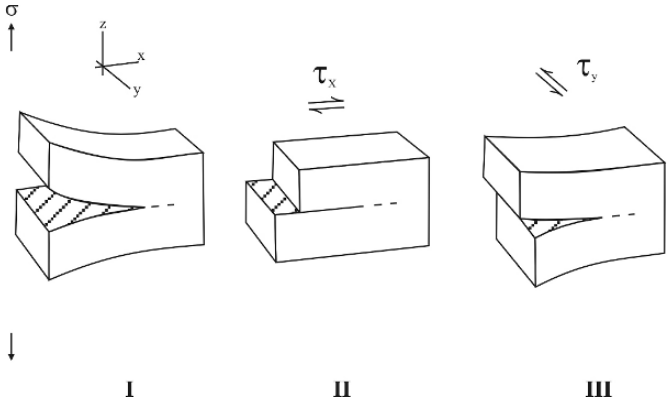


**Figure 4.29** The three basic modes of distortion at a crack tip (after Paterson, 1978).

### *4.5.4 Fracture mechanics*

Griffith's energy instability concept forms the basis of the engineering science of fracture mechanics which is being used increasingly to study a number of fracture propagation phenomena in rock mechanics. The outline of the essential concepts of fracture mechanics given here follows that of Paterson (1978).

Although, as illustrated in Figure 4.25, non-elastic effects operate at the tips of cracks in rock, the practical analysis of the stresses in the vicinity of a crack tip is usually carried out using the classical theory of linear elasticity. In this case, the approach is referred to as **linear elastic fracture mechanics**. The purpose of this stress analysis is to estimate the "loading" applied to the crack tip and to determine whether or not the crack will propagate. In order to do this, the nature of the stress distribution in the vicinity of the crack tip must be determined.

The analysis of the stresses in the vicinity of the crack tip is approached by considering three basic modes of distortion, designated modes I, II and III, and defined with respect to a reference plane that is normal to the edge of a straight line crack. As shown in Figure 4.29, modes I and II are the plane strain distortions in which the points on the crack surface are displaced in the reference plane normal and parallel, respectively, to the plane of the crack. Mode III is the anti-plane strain distortion in which the points on the crack surface are displaced normal to the reference plane. In simpler terms, modes I, II and III are the extension or opening, in-plane shear and out-of-plane shear modes, respectively. The stress and displacement fields around the crack tip in these three basic modes of distortion are obtained by considering the distributions resulting from the application of uniform loadings at infinity. In the absence of perturbations due to the crack, these loadings correspond, respectively, to a uniform tensile stress normal to the crack (I), a uniform shear stress parallel to the crack (II) and a uniform shear stress transverse to the crack (III).

It is found that, for each mode of distortion, each of the stress and displacement components can be expressed as the product of a spatial distribution function that is independent of the actual value of the applied stress and a scaling factor that depends only on the applied stress and the crack length. The same scaling factor applies for each of the stress and displacement components in a given mode. It is known as the **stress intensity factor** for that mode. The stress intensity factors for the three modes of distortion are designated $K_I$, $K_{II}$ and $K_{III}$, respectively. For example, in the mode I case for the co-ordinate axes shown in Figure 4.29, the $\sigma_{zz}$ stress component near the

crack tip within the material in the plane of the crack is given by (Jaeger and Cook, 1979)

$$\sigma_{zz} = \sigma\sqrt{(c/2x)}$$

or,

$$\sigma_{zz} = K_1/\sqrt{(2\pi x)} \tag{4.22}$$

where $K_I = \sigma\sqrt{(\pi c)}$, 2c is the crack length, $x$ is the distance from the crack tip and $\sigma$ is the far field stress applied normal to the crack. Equations of a similar form to equation 4.22 may be obtained for the other modes of distortion (e.g. Paris and Sih, 1965).

It is clear from the above that the values of $K_I$, $K_{II}$ and $K_{III}$ in any particular case depend on both the macroscopic stress field and the geometry of the specimen. These values have been calculated for a number of practical cases (e.g. Paris and Sih, 1965, Whittaker *et al.,* 1992). The question then arises as to when a crack in a particular case will begin to extend. In linear elastic fracture mechanics, it is postulated that the crack will begin to extend when a critical intensity of loading as measured by the stress intensity factors is reached at its tip. That is, the failure criterion is expressed in terms of **critical stress intensity factors** designated $K_{IC}$, $K_{IIC}$, $K_{IIIC}$. These factors which are also known as **fracture toughnesses** are regarded as material properties. Practical procedures have been developed for measuring them for a range of engineering materials including rock (e.g. Backers *et al.*, 2002, ISRM Testing Commission 1988, 1995, Whittaker *et al.,* 1992.) It must be noted that in many practical problems, the applied stress field will be such that a mixed mode of fracture will apply.

### *4.5.5 Empirical criteria*

Because the classic strength theories used for other engineering materials have been found not to apply to rock over a wide range of applied compressive stress conditions, a number of empirical strength criteria have been introduced for practical use. These criteria usually take the form of a power law in recognition of the fact that peak $\sigma_1$ vs. $\sigma_3$ and $\tau$ vs. $\sigma_n$ envelopes for rock material are generally concave downwards (Figures 4.21, 30, and 31). In order to ensure that the parameters used in the power laws are dimensionless, these criteria are best written in normalised form with all stress components being divided by the uniaxial compressive strength of the rock.

Bieniawski (1974) found that the peak triaxial strengths of a range of rock types were well represented by the criterion

$$\frac{\sigma_1}{\sigma_c} = 1 + A\left(\frac{\sigma_3}{\sigma_c}\right)^k \tag{4.23}$$

or

$$\frac{\tau_m}{\sigma_c} = 0.1 + B\left(\frac{\sigma_m}{\sigma_c}\right)^c \tag{4.24}$$

where $\tau_m = \frac{1}{2}(\sigma_1 - \sigma_3)$ and $\sigma_m = \frac{1}{2}(\sigma_1 + \sigma_3)$.

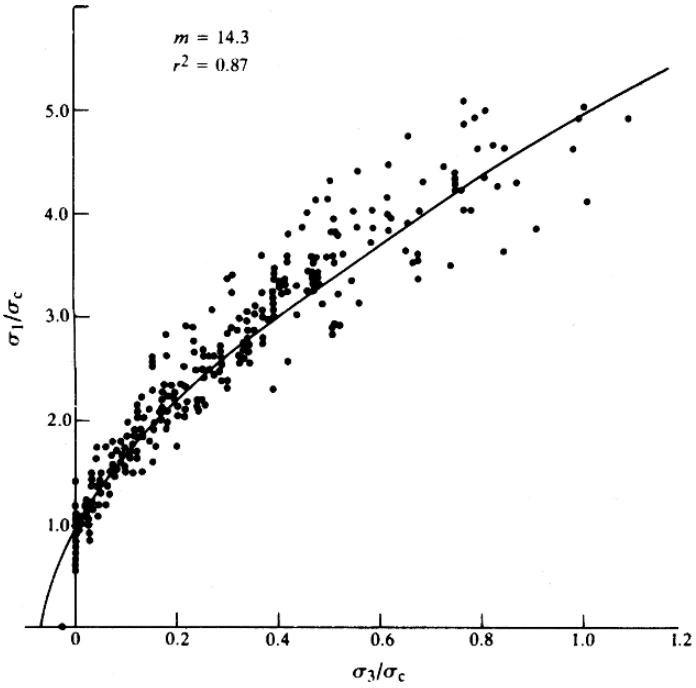


**Figure 4.30** Normalised peak strength envelope for sandstones (after Hoek and Brown, 1980).

Bieniawski found that, for the range of rock types tested, $k \simeq 0.75$ and $c \simeq 0.90$. The corresponding values of $A$ and $B$ are given in Table 4.1. Note that both $A$ and $B$ take relatively narrow ranges for the rock types tested.

Brady (1977) studied the development of rock fracture around a bored raise in a pillar in mineralised shale in a trial stoping block at the Mount Isa Mine, Australia.

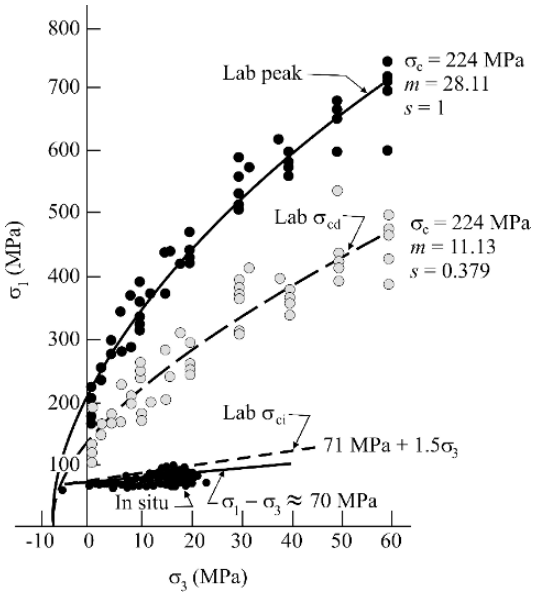


**Figure 4.31** Hoek-Brown failure envelope for Lac du Bonnet granite based on laboratory peak strength (Lab Peak), long-term strength (Lab $\sigma_{cd}$) and *in situ* crack initiation stress ($\sigma_{ci}$) determined by microseismic monitoring (after Martin, 1997).

**Table 4.1** Constants in Bieniawski's empirical strength criterion (after Bieniawski, 1974).

| Rock type | A | B |
|---|---|---|
| norite | 5.0 | 0.8 |
| quartzite | 4.5 | 0.78 |
| sandstone | 4.0 | 0.75 |
| siltstone | 3.0 | 0.70 |
| mudstone | 3.0 | 0.70 |

Using a boundary element analysis to calculate the elastic stresses induced around the raise as the pillar was progressively mined, he found that fracture of the rock could be accurately modelled using equation 4.23 with $A = 3.0$, $k = 0.75$ and $\sigma_c = 90$ MPa which is approximately half the mean value of 170 MPa measured in laboratory tests.

Hoek and Brown (1980) found that the peak triaxial compressive strengths of a wide range of isotropic rock materials could be described by the equation

$$\sigma_1 = \sigma_3 + \left(m\ \sigma_c\ \sigma_3 + s\sigma_c^2\right)^{0.5} \tag{4.25}$$

where $m$ varies with rock type and $s = 1.0$ for intact rock material. On the basis of analyses of published strength data and some interpolation and extrapolation based on practical experience, Marinos and Hoek (2000) have suggested that the constant m for intact rock, $m_i$, varies with rock type in the manner shown in Table 4.2.

A normalised peak strength envelope for sandstones is shown in Figure 4.30. The grouping and analysis of data according to rock type has obvious disadvantages. Detailed studies of rock strength and fracture indicate that factors such as mineral composition, grain size and angularity, grain packing patterns and the nature of cementing materials between grains, all influence the manner in which fracture initiates and propagates. If these factors are relatively uniform within a given rock type, then it might be expected that a single curve would give a good fit to the normalised strength data with a correspondingly high value of the coefficient of determination, $r^2$. If, on the other hand, these factors are quite variable from one occurrence of a given rock type to another, then a wider scatter of data points and a poorer fit by a single curve might be anticipated. For sandstones (Figure 4.30) where grain size, porosity and the nature of the cementing material can vary widely, and for limestone which is a name given to a wide variety of carbonate rocks, the values of $r^2$ are, indeed, quite low.

Despite these difficulties and the sometimes arbitrary allocation of a particular name to a given rock, the results obtained initially by Hoek and Brown (1980) and updated by Marinos and Hoek (2000), do serve an important practical purpose. By using the approximate value of $m_i$ found to apply for a particular rock type, it may be possible to carry out preliminary design calculations on the basis of no testing other than a determination of a suitable value of $\sigma_c$ made using a simple test such as the point load test. A value of $\sigma_c$ is required as a scaling factor to determine the strength of a particular sample of rock. Thus although the same value of $m_i$ may apply to granites from different localities, their strengths at different confining pressures may differ by a factor of two or three.

**Table 4.2** Variation of the constant $m_i$ for intact rock by rock group (after Hoek, 2003).

| | Rock Type | Class | Group | Texture | | | |
|---|---|---|---|---|---|---|---|
| | | | | Coarse | Medium | Fine | Very fine |
| SEDIMENTARY | | Clastic | | Conglomerates* Breccias* | Sandstones 17± 4 | Siltstones 7 ± 2 Greywackes (18 ± 3) | Claystones 4 ± 2 Shales (6± 2) Maris (7 ± 2) |
| | | Non-Clastic | Carbonates | Crystalline Limestone (12 ± 3) | Sparitic Limestones (10 ± 2) | Micritic Limestones (9 ± 2) | Dolomites (9 ± 3) |
| | | | Evaporites | | Gypsum 8 ± 2 | Anhydrite 12 ± 2 | |
| | | | Organic | | | | Chalk 7 ± 2 |
| METAMORPHIC | | Non Foliated | | Marble 9 ± 3 | Hornfels (19 ± 4) Metasandstone (19 ± 3) | Quartzites 20 ± 3 | |
| | | Slightly foliated | | Migmatite (29 ± 3) | Amphibolites 26 ± 6 | Gneiss 28 ± 5 | |
| | | Foliated ** | | | Schists 12 ± 3 | Phyllites (7 ± 3) | Slates 7 ± 4 |
| IGNEOUS | | Plutonic | Light | Granite 32 ± 3 | Diorite 25 ± 5 | | |
| | | | | Granodiorite (29 ± 3) | | | |
| | | | Dark | Gabbro 27 ± 3 | Dolerite (16 ± 5) | | |
| | | | | Norite 20 ± 5 | | | |
| | | Hypabyssal | | Porphyries (20 ± 5) | | Diabase (15 ± 5) | Periodotite (25 ± 5) |
| | | Volcanic | Lava | | Rhyolite (25 ± 5) Andesite 25 ± 5) | Dacite (25 ± 3) Basalt (25 ± 5) | |
| | | | Pyroclastic | Agglomerate (19 ± 3) | Breccia (19 ± 5) | Tuff (13 ± 5) | |

*Conglomerates and breccias may present a wide range of $m_i$ values depending on the nature of the cementing material and the degree of cementation, so they may range from values similar to sandstone, to values used for fine grained sediments (even under 10).

**These values are for intact rock specimens tested normal to bedding or foliation. The value of $m_i$ will be significantly different if failure occurs along a weakness plane.

An instructive and practically useful interpretation of the Hoek-Brown criterion for brittle intact rock has been provided by Martin (1997) and others (e.g. Martin and Chandler, 1994, Hajiabdolmajid *et al.,* 2002, Martin *et al.,* 1999), who studied the laboratory and field behaviour of Lac du Bonnet granite. Martin (1997) found that, in a manner consistent with that described in Section 4.3.7, the start of the fracture or failure process began with the initiation of damage caused by small cracks growing in the direction of the maximum applied load. For unconfined Lac du Bonnet granite, this occurred at an applied stress of 0.3 to 0.4 $\sigma_c$. As the load increased, these stable cracks continued to accumulate. Eventually, when the sample contained a sufficient density of these cracks, they started to interact and an unstable cracking process involving sliding was initiated. The stress level at which this unstable cracking process is initiated is referred to as the **long term strength** of the rock, $\sigma_{cd}$. Martin (1997) argued that, in terms of the Coulombic concepts of cohesion and friction, the mobilised strength to this stage is cohesive. After the stress $\sigma_{cd}$ has been reached, cohesion is lost and frictional strength is mobilised.

As illustrated in Figure 4.31, Martin (1997) determined the laboratory peak, long term and crack initiation strengths for the Lac du Bonnet granite. He was able to fit Hoek-Brown failure envelopes to these curves, although the laboratory crack initiation curve was found to be a straight line on $\sigma_1$ versus $\sigma_3$ axes. Subsequently, in a field experiment carried out at the URL site, the initiation of cracks around a tunnel excavated in the Lac du Bonnet granite was recorded using microseismic emissions (see section 18.2.7). As shown in Figure 4.31, these data correspond well with the laboratory crack initiation data. It was found that crack initiation at approximately constant deviatoric stress, $(\sigma_1 - \sigma_3)$, could be well represented by the Hoek-Brown criterion with $m_b = 0$ and $s = 0.11$ (Martin *et al.,* 1999). This important result will be used in later chapters of this book.

### *4.5.6 Yield criteria based on plasticity theory*

The incremental theory of plasticity (Hill, 1950) is a branch of continuum mechanics that was developed in an attempt to model analytically the plastic deformation or flow of metals. Plastic deformation is permanent or irrecoverable; its onset marks the yield point. Perfectly plastic deformation occurs at constant volume under constant stress. If an increase in stress is required to produce further post-yield deformation, the material is said to be work- or strain-hardening.

As noted in section 4.4.3, plastic or dissipative mechanisms of deformation may occur in rocks under suitable environmental conditions. It would seem reasonable, therefore, to attempt to use plasticity theory to develop yield criteria for rocks. The relevant theory is beyond the scope of this introductory text and only the elements of it will be introduced here.

Because plastic deformation is accompanied by permanent changes in atomic positions, plastic strains cannot be defined uniquely in terms of the current state of stress. Plastic strains depend on loading history, and so plasticity theory must use an incremental loading approach in which incremental deformations are summed to obtain the total plastic deformation. In some engineering problems, the plastic strains are much larger than the elastic strains, which may be neglected. This is not always the case for rock deformation (for example, Elliott and Brown, 1985), and so an elastoplastic analysis may be required.

The total strain increment $\{\dot{\varepsilon}\}$ is the sum of the elastic and plastic strain increments

$$\{\dot{\varepsilon}\} = \{\dot{\varepsilon}^{e}\} + \{\dot{\varepsilon}^{p}\} \tag{4.26}$$

A plastic potential function, $Q$ ($\{\sigma\}$), is defined such that

$$\{\dot{\varepsilon}^{p}\} = \lambda \left\{ \frac{\partial Q}{\partial \sigma} \right\} \tag{4.27}$$

where $\lambda$ is a non-negative constant of proportionality which may vary throughout the loading history. Thus, from the incremental form of equation 2.38 and equations 4.26 and 4.27

$$\{\dot{\varepsilon}\} = [\mathbf{D}]^{-1}\{\dot{\sigma}\} + \lambda \left\{ \frac{\partial Q}{\partial \sigma} \right\} \tag{4.28}$$

where $[\mathbf{D}]$ is the elasticity matrix.

It is also necessary to be able to define the stress states at which yield will occur and plastic deformation will be initiated. For this purpose, a yield function, $F(\{\sigma\})$, is defined such that $F = 0$ at yield. If $Q = F$, the flow law is said to be associated. In this case, the vectors of $\{\sigma\}$ and $\{\dot{\varepsilon}^{p}\}$ are orthogonal as illustrated in Figure 4.32. This is known as the normality condition.

For isotropic hardening and associated flow, elastoplastic stress and strain increments may be related by the equation

$$\{\dot{\sigma}\} = [\mathbf{D}^{ep}][\dot{\varepsilon}]$$

where

$$[\mathbf{D}^{ep}] = [\mathbf{D}] - \frac{[\mathbf{D}]\left\{\frac{\partial Q}{\partial \sigma}\right\}\left\{\frac{\partial F}{\partial \sigma}\right\}^{T}[\mathbf{D}]}{A + \left\{\frac{\partial F}{\partial \sigma}\right\}^{T}[\mathbf{D}]\left\{\frac{\partial Q}{\partial \sigma}\right\}}$$

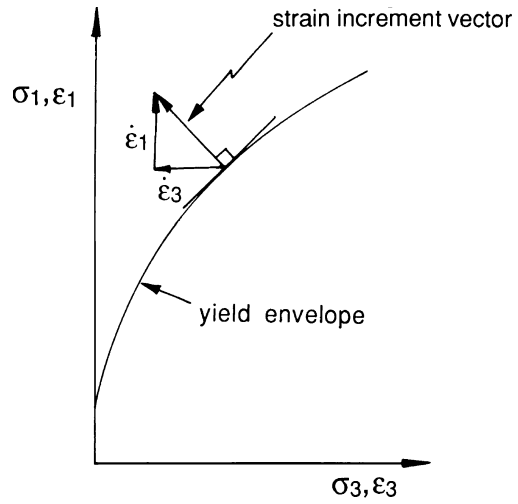


**Figure 4.32** The normality condition of the associated flow rule.

in which

$$A = -\frac{1}{\lambda}\frac{\partial F}{\partial K}\mathrm{d}K$$

where $K$ is a hardening parameter such that yielding occurs when

$$\mathrm{d}F = \left\{\frac{\partial F}{\partial \sigma}\right\}^{\mathrm{T}}\{\dot{\sigma}\} + \frac{\partial F}{\partial K} = 0$$

The concepts of associated plastic flow were developed for perfectly plastic and strain-hardening metals using yield functions such as those of Tresca and von Mises which are independent of the hydrostatic component of stress (Hill, 1950). Although these concepts have been found to apply to some geological materials, it cannot be assumed that they will apply to pressure-sensitive materials such as rocks in which brittle fracture and dilatancy typically occur (Rudnicki and Rice, 1975).

In order to obtain realistic representations of the stresses at yield in rocks and rock masses, it has been necessary to develop yield functions which are more complex than the classical functions introduced for metals. These functions are often of the form $F(I_1, J_2) = 0$ where $I_1$ is the first invariant of the stress tensor and $J_2$ is the second invariant of the deviator stress tensor (section 2.4), i.e.

$$\begin{aligned} J_2 &= \tfrac{1}{2}\left(S_1^2 + S_2^2 + S_3^2\right) \\ &= \tfrac{1}{6}[(\sigma_1 - \sigma_2)^2 + (\sigma_2 - \sigma_3)^2 + (\sigma_3 - \sigma_1)^2] \end{aligned}$$

More complex functions also include the third invariant of the deviator stress tensor $J_3 = S_1\ S_2\ S_3$. For example, Desai and Salami (1987) were able to obtain excellent fits to peak strength (assumed synonymous with yield) and stress–strain data for a sandstone, a granite and a dolomite using the yield function

$$F = J_2 - \left(\frac{\alpha}{\alpha_0^{n-2}}\ I_1^n + I_1^2\right)\left(1 - \beta\frac{J_3^{1/3}}{J_2^{1/2}}\right)^m$$

where $\alpha$, $n$, $\beta$ and $m$ are material parameters and $\alpha_0$ is one unit of stress.

## 4.6 Strength of anisotropic rock material in triaxial compression

So far in this chapter, it has been assumed that the mechanical response of rock material is isotropic. However, because of some preferred orientation of the fabric or microstructure, or the presence of bedding or cleavage planes, the behaviour of many rocks is anisotropic. The various categories of anisotropic elasticity were discussed in section 2.10. Because of computational complexity and the difficulty of determining the necessary elastic constants, it is usual for only the simplest form of anisotropy, transverse isotropy, to be used in design analyses. Anisotropic strength criteria are also required for use in the calculations.

The peak strengths developed by transversely isotropic rocks in triaxial compression vary with the orientation of the plane of isotropy, foliation plane or plane of weakness, with respect to the principal stress directions. Figure 4.33 shows some

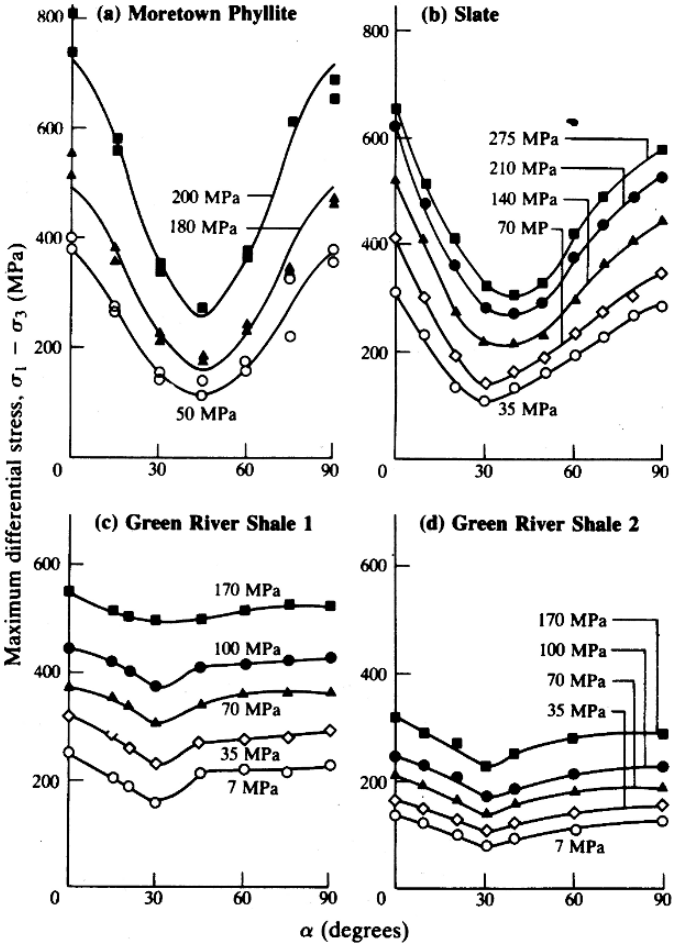


**Figure 4.33** Variation of peak principal stress difference with the angle of inclination of the major principal stress to the plane of weakness, for the confining pressures indicated for (a) a phyllite (after Donath, 1972), (b–d) a slate and two shales (after McLamore and Gray, 1967).

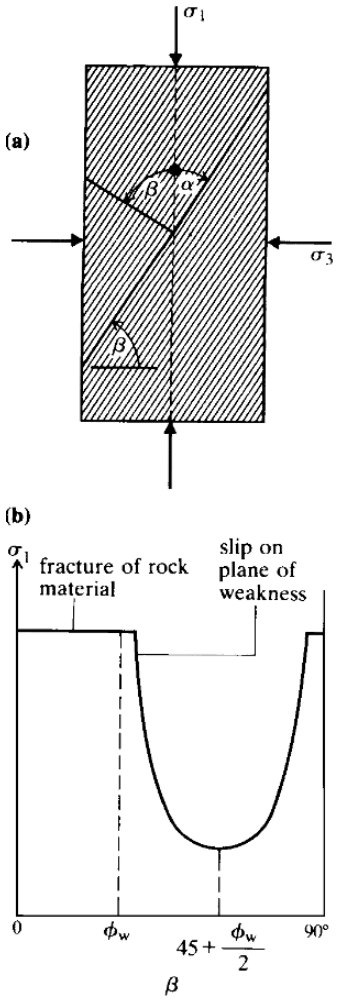


**Figure 4.34** (a) Transversely isotropic specimen in triaxial compression; (b) variation of peak strength at constant confining pressure with the angle of inclination of the normal to the plane of weakness to the compression axis ($\beta$).

measured variations in peak principal stress difference with the angle of inclination of the major principal stress to the plane of weakness.

Jaeger (1960) introduced an instructive analysis of the case in which the rock contains well-defined, parallel planes of weakness whose normals are inclined at an angle $\beta$ to the major principal stress direction as shown in Figure 4.34a. Each plane of weakness has a limiting shear strength defined by Coulomb's criterion

$$s = c_w + \sigma_n \tan \phi_w \tag{4.29}$$

Slip on the plane of weakness ($ab$) will become incipient when the shear stress on the plane, $\tau$, becomes equal to, or greater than, the shear strength, $s$. The stress transformation equations give the normal and shear stresses on $ab$ as

$$\sigma_n = \tfrac{1}{2}(\sigma_1 + \sigma_3) + \tfrac{1}{2}(\sigma_1 - \sigma_3)\cos 2\beta$$

and

$$\tau = \tfrac{1}{2}(\sigma_1 - \sigma_3)\sin 2\beta \tag{4.30}$$

Substituting for $\sigma_n$ in equation 4.29, putting $s = \tau$, and rearranging, gives the criterion for slip on the plane of weakness as

$$(\sigma_1 - \sigma_3)_s = \frac{2(c_w + \sigma_3 \tan \phi_w)}{(1 - \tan \phi_w \cot \beta) \sin 2\beta} \tag{4.31}$$

The principal stress difference required to produce slip tends to infinity as $\beta \to 90^\circ$ and as $\beta \to \phi_w$. Between these values of $\beta$, slip on the plane of weakness is possible, and the stress at which slip occurs varies with $\beta$ according to equation 4.31. By differentiation, it is found that the minimum strength occurs when

$$\tan 2\beta = -\cot \phi_w$$

or when

$$\beta = \frac{\pi}{4} + \frac{\phi_w}{2}$$

The corresponding value of the principal stress difference is

$$(\sigma_1 - \sigma_3)_{min} = 2(c_w + \mu_w \sigma_3)\left(\left[1 + \mu_w^2\right]^{1/2} + \mu_w\right)$$

where $\mu_w = \tan \phi_w$.

For values of $\beta$ approaching $90^\circ$ and in the range $0^\circ$ to $\phi_w$, slip on the plane of weakness cannot occur, and so the peak strength of the specimen for a given value of $\sigma_3$, must be governed by some other mechanism, probably shear fracture through the rock material in a direction not controlled by the plane of weakness. The variation of peak strength with the angle $\beta$ predicted by this theory is illustrated in Figure 4.34b.

Note that the peak strength curves shown in Figure 4.33, although varying with $\beta$ and showing pronounced minima, do not take the same shape as Figure 4.34b. (In comparing these two figures note that the abscissa in Figure 4.33 is $\alpha = \pi/2 - \beta$). In particular, the plateau of constant strength at low values of $\alpha$, or high values of $\alpha$, predicted by the theory, is not always present in the experimental strength data. This suggests that the two-strength model of Figure 4.34 provides an oversimplified representation of strength variation in anisotropic rocks. Such observations led Jaeger (1960) to propose that the shear strength parameter, $c_w$, is not constant but is continuously variable with $\beta$ or $\alpha$. McLamore and Gray (1967) subsequently proposed that both $c_w$ and $\tan \phi_w$ vary with orientation according to the empirical relations

$$c_w = A - B[\cos 2(\alpha - \alpha_{c0})]^n$$

and

$$\tan \phi_w = C - D[\cos 2(\alpha - \alpha_{\phi 0})]^m$$

where $A$, $B$, $C$, $D$, $m$ and $n$ are constants, and $\alpha_{c0}$ and $\alpha_{\phi 0}$ are the values of $\alpha$ at which $c_w$ and $\phi_w$ take minimum values, respectively.

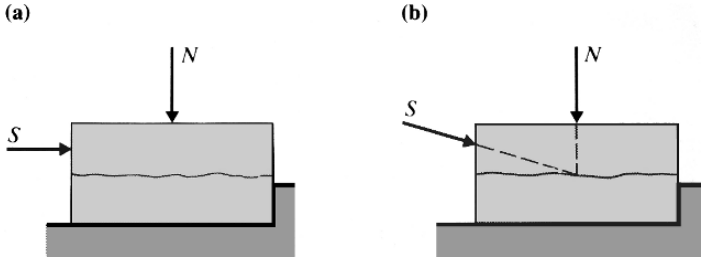


**Figure 4.35** Direct shear test configurations with (a) the shear force applied parallel to the discontinuity, (b) an inclined shear force.

## 4.7 Shear behaviour of discontinuities

### *4.7.1 Shear testing*

In mining rock mechanics problems other than those involving only fracture of intact rock, the shear behaviour of discontinuities will be important. Conditions for slip on major pervasive features such as faults or for the sliding of individual blocks from the boundaries of excavations are governed by the shear strengths that can be developed by the discontinuities concerned. In addition, the shear and normal stiffnesses of discontinuities can exert a controlling influence on the distribution of stresses and displacements within a discontinuous rock mass. These properties can be measured in the same tests as those used to determine discontinuity shear strengths.

The most commonly used method for the shear testing of discontinuities in rock is the **direct shear test**. As shown in Figure 4.35, the discontinuity surface is aligned parallel to the direction of the applied shear force. The two halves of the specimen are fixed inside the shear box using a suitable encapsulating material, generally an epoxy resin or plaster. This type of test is commonly carried out in the laboratory, but it may also be carried out in the field, using a **portable shear box** to test discontinuities contained in pieces of drill core or as an *in situ* test on samples of larger size. Methods of preparing samples and carrying out these various tests are discussed by the ISRM Commission (1974), Goodman (1976, 1989) and Hoek and Bray (1981).

Test arrangements of the type shown in Figure 4.35a can cause a moment to be applied about a lateral axis on the discontinuity surface. This produces relative rotation of the two halves of the specimen and a non-uniform distribution of stress over the discontinuity surface. To minimise these effects, the shear force may be inclined at an angle (usually 10°–15°) to the shearing direction as shown in Figure 4.35b. This is almost always done in the case of large-scale *in situ* tests. Because the mean normal stress on the shear plane increases with the applied shear force up to peak strength, it is not possible to carry out tests in this configuration at very low normal stresses.

Direct shear tests in the configuration of Figure 4.35a are usually carried out at constant normal force or constant normal stress. Tests are most frequently carried out on dry specimens, but many shear boxes permit specimens to be submerged and drained shear tests to be carried out with excess joint water pressures being assumed to be fully dissipated throughout the test. Undrained testing with the measurement of induced joint water pressures, is generally not practicable using the shear box.

The **triaxial cell** is sometimes used to investigate the shear behaviour of discontinuities. Specimens are prepared from cores containing discontinuities inclined at 25–40° to the specimen axis. A specimen is set up in the triaxial cell as shown in Figure 4.34a for the case of anisotropic rocks, and the cell pressure and the axial load

are applied successively. The triaxial cell is well suited to testing discontinuities in the presence of water. Tests may be either drained or undrained, preferably with a known level of joint water pressure being imposed and maintained throughout the test.

It is assumed that slip on the discontinuity will occur according to the theory set out in section 4.6. Mohr circle plots are made of the total or effective stresses at slip at a number of values of $\sigma_3$, and the points on these circles giving the stresses on the plane of the discontinuity are identified. The required shear strength envelope is then drawn through these points. This requires that a number of tests be carried out on similar discontinuities.

In an attempt to overcome the need to obtain, prepare and set up several specimens containing similar discontinuities, a **stage testing** procedure is sometimes used. A specimen is tested at a low confining pressure as outlined above. When it appears that slip on the discontinuity has just been initiated (represented by a flattening of the axial load–axial displacement curve that must be continuously recorded throughout each test), loading is stopped, the cell pressure is increased to a new value, and loading is recommenced. By repeating this process several times, a number of points on the peak strength envelope of the discontinuity can be obtained from the one specimen. However, this approach exacerbates the major difficulty involved in using the triaxial test to determine discontinuity shear strengths, namely the progressive change in the geometry of the cell–specimen system that accompanies shear displacement on the discontinuity.

The problem is illustrated by Figure 4.36. It is clear from Figure 4.36a that, if relative shear displacement of the two parts of the specimen is to occur, there must be lateral as well as axial relative translation. If, as is often the case, one spherical seat is used in the system, axial displacement causes the configuration to change to that of Figure 4.36b, which is clearly unsatisfactory. As shown in Figure 4.36c, the use of two spherical seats allows full contact to be maintained over the sliding surfaces, but the area of contact changes and frictional and lateral forces are introduced at the seats. Figure 4.36d illustrates the most satisfactory method of ensuring that the lateral component of translation can occur freely and that contact of the discontinuity surfaces is maintained. Pairs of hardened steel discs are inserted between the platens and either end of the specimen. No spherical seats are used. The surfaces forming the interfaces between the discs are polished and lubricated with a molybdenum disulphide grease.

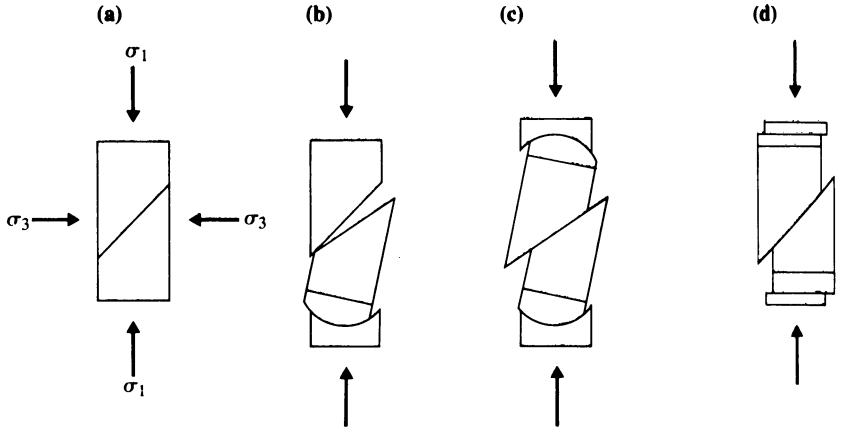


**Figure 4.36** Discontinuity shear testing in a triaxial cell (after Jaeger and Rosengren, 1969).

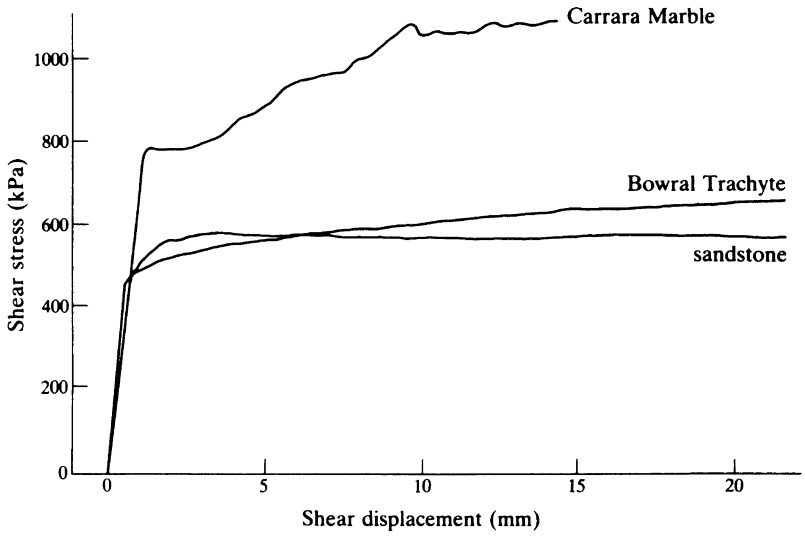


**Figure 4.37** Shear stress–shear displacement curves for ground surfaces tested with a constant normal stress of 1.0 MPa (after Jaeger, 1971).

In this way, the coefficient of friction between the plates can be reduced to the order of 0.005 which allows large amounts of lateral displacement to be accommodated at the interface with little resistance.

This technique was developed by Rosengren (1968) who determined the corrections required to allow for the influence of friction and the change of contact area. His analysis has been re-presented by Goodman (1976, 1989) and will not be repeated here. The authors have successfully used this technique in tests on specimens of 150 mm diameter tested at confining pressures of up to 70 MPa.

### *4.7.2 Influence of surface roughness on shear strength*

Shear tests carried out on smooth, clean discontinuity surfaces at constant normal stress generally give shear stress–shear displacement curves of the type shown in Figure 4.37. When a number of such tests are carried out at a range of effective normal stresses, a linear shear strength envelope is obtained (Figure 4.38). Thus the shear strength of smooth, clean discontinuities can be described by the simple Coulomb law

$$s = \sigma_n' \tan \phi' \tag{4.32}$$

where $\phi'$ is the effective angle of friction of the discontinuity surfaces. For the case shown in Figure 4.38, $\phi' = 35^\circ$, a typical value for quartz-rich rocks.

Naturally occurring discontinuity surfaces are never as smooth as the artificially prepared surfaces which gave the results shown in Figures 4.38 and 4.39. The shear force–shear displacement curve shown in Figure 4.39a is typical of the results obtained for clean, rough discontinuities. The peak **strength** at constant normal stress is reached after a small shear displacement. With further displacement, the shear resistance falls until the **residual strength** is eventually reached. Tests at a number of normal stresses give peak and residual strength envelopes such as those shown in Figure 4.40.

This behaviour can be explained in terms of surface roughness using a simple model introduced by Patton (1966) (Figure 4.41). A smooth, clean, dry discontinuity

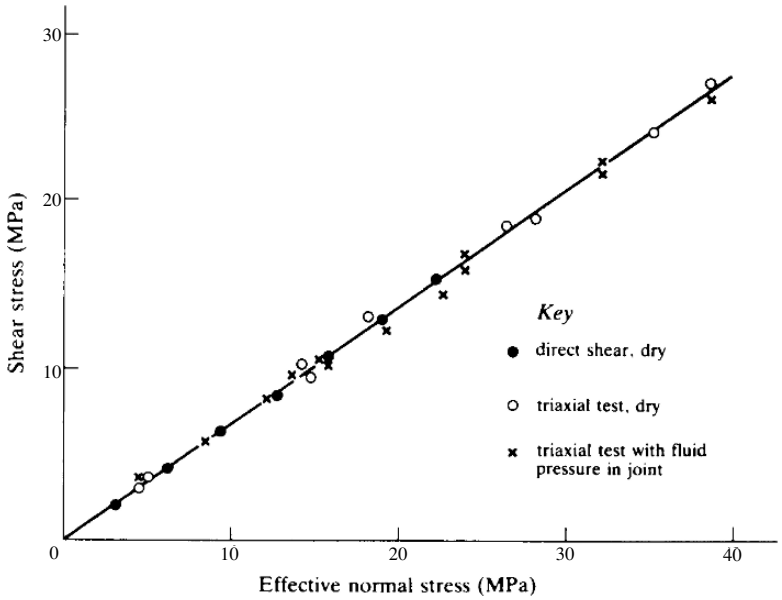


**Figure 4.38** Sliding of smooth quartzite surfaces under various conditions (after Jaeger and Rosengren, 1969).

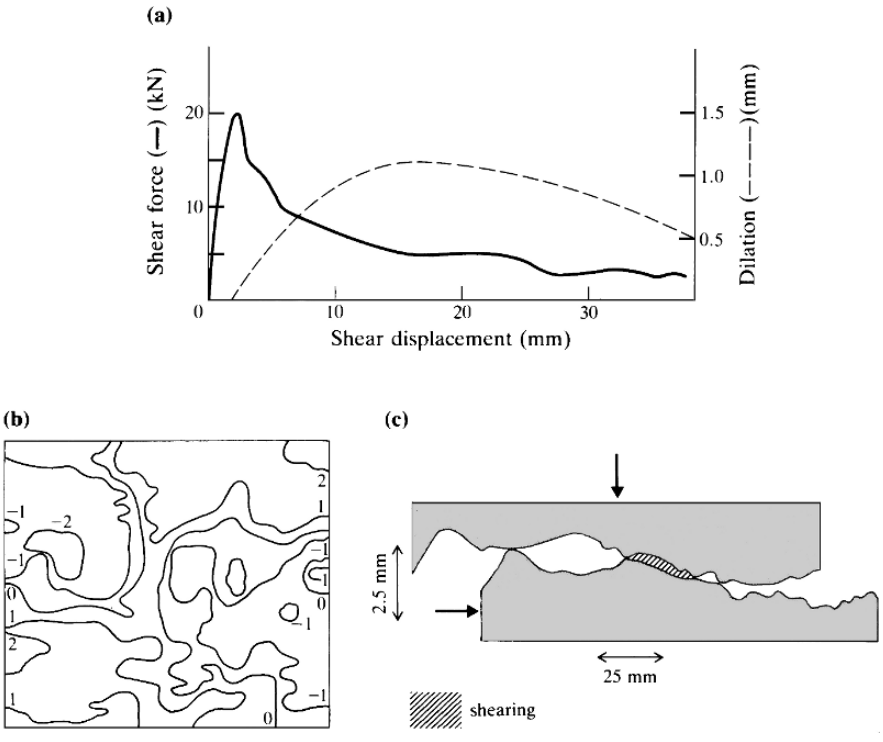


**Figure 4.39** Results of a direct shear test on a 127 mm × 152 mm graphite-coated joint, carried out at a constant normal force of 28.9 kN. (a) Shear force–shear displacement curves; (b) surface profile contours before testing (mm); (c) relative positions on a particular cross section after 25 mm of sliding (after Jaeger, 1971).

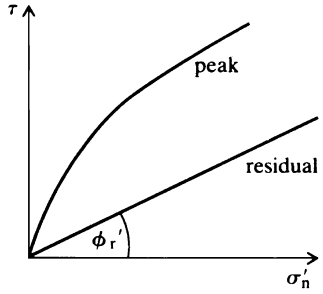


**Figure 4.40** Peak and residual effective stress shear strength envelopes.

surface has a friction angle $\phi$, so that at limiting equilibrium for the direct shear test configuration of Figure 4.41a,

$$\frac{S}{N} = \tan \phi$$

If the discontinuity surface is inclined at an angle $i$ to the direction of the shear force, $S$ (Figure 4.41b), then slip will occur when the shear and normal forces on the discontinuity, $S^*$ and $N^*$, are related by

$$\frac{S^*}{N^*} = \tan \phi \tag{4.33}$$

Resolving $S$ and $N$ in the direction of the discontinuity surface gives

$$S^* = S \cos i - N \sin i$$

and

$$N^* = N \cos i + S \sin i$$

Substitution of these values in equation 4.33 and simplification gives the condition for slip as

$$\frac{S}{N} = \tan (\phi + i) \tag{4.34}$$

Thus the inclined discontinuity surface has an apparent friction angle of $(\phi + i)$. Patton extended this model to include the case in which the discontinuity surface contains a number of 'teeth' (Figure 4.41c and d). In a series of model experiments

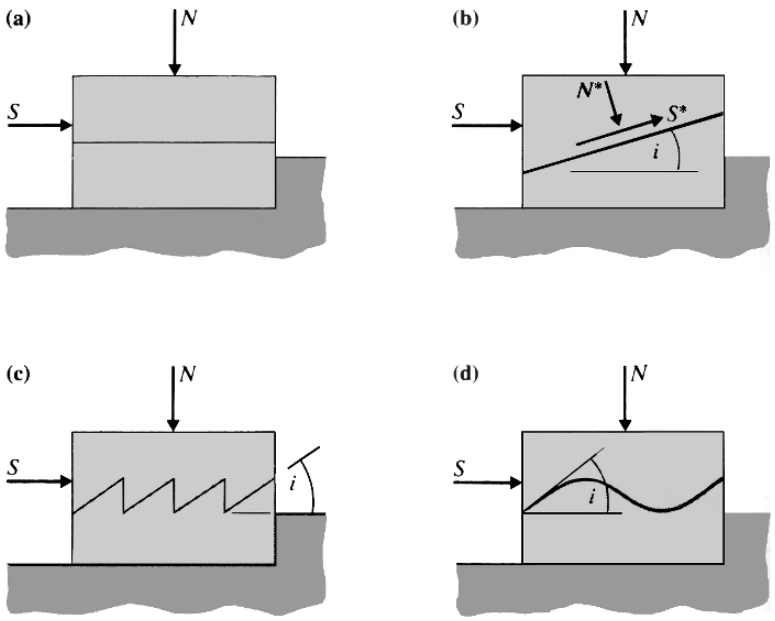


**Figure 4.41** Idealised surface roughness models illustrating the roughness angle, $i$.

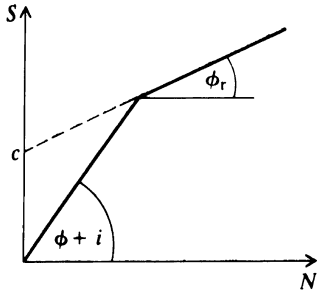


**Figure 4.42** Bilinear peak strength envelope obtained in direct shear tests on the models shown in Figure 4.41.

with a variety of surface profiles, he found that, at low values of $N$, sliding on the inclined surfaces occurred according to equation 4.34. Dilation of the specimens necessarily accompanied this mechanism. As the value of $N$ was increased above some critical value, sliding on the inclined asperity surfaces was inhibited, and a value of $S$ was eventually reached at which shear failure through the asperities occurred. The corresponding values of $S$ and $N$ gave the upper portion of the bilinear shear strength envelope shown in Figure 4.42. Note that, in such cases, the shear strengths that can be developed at low normal loads can be seriously overestimated by extrapolating the upper curve back to $N = 0$ and using a Coulomb shear strength law with a cohesion intercept, $c$, and a friction angle, $\phi_r$.

Natural discontinuities rarely behave in the same way as these idealised models. However, the same two mechanisms – sliding on inclined surfaces at low normal loads and the suppression of dilation and shearing through asperities at higher normal loads – are found to dominate natural discontinuity behaviour. Generally, the two mechanisms are combined in varying proportions with the result that peak shear strength envelopes do not take the idealised bilinear form of Figure 4.42 but are curved. These combined effects are well illustrated by the direct shear test on a graphite-coated joint which gave the results shown in Figure 4.39a. The roughness profile of the initially mating surfaces is shown in Figure 4.39b. The maximum departure from the mean plane over the 127 mm $\times$ 152 mm surface area was in the order of $\pm$ 2.0 mm. After 25 mm of shear displacement at a constant normal force of 28.9 kN, the relative positions of the two parts of the specimen were as shown in Figure 4.39c. Both riding up on asperities and shearing off of some material in the shaded zone took place.

Roughness effects can cause shear strength to be a directional property. Figure 4.43 illustrates a case in which rough discontinuity surfaces were prepared in slate specimens by fracturing them at a constant angle to the cleavage. When the specimens were tested in direct shear with the directions of the ridges on the surfaces parallel to the direction of sliding (test A), the resulting shear strength envelope gave an effective friction angle of 22° which compares with a value of 19.5° obtained for clean, polished surfaces. However, when the shearing direction was normal to the ridges (test B), sliding up the ridges occurred with attendant dilation. A curved shear strength envelope was obtained with a roughness angle of 45.5° at near zero effective normal stress and a roughness angle of 24° at higher values of effective normal stress.

### *4.7.3 Interrelation between dilatancy and shear strength*

All of the test data presented in the previous section were obtained in direct shear tests carried out at constant normal force or stress. Because of the influence of surface roughness, dilatancy accompanies shearing of all but the smoothest discontinuity surfaces in such tests. Goodman (1976, 1989) pointed out that although this test may reproduce discontinuity behaviour adequately in the case of sliding of an unconstrained block of rock from a slope (Figure 4.44c), it may not be suited to the determination of the stress–displacement behaviour of discontinuities isolating a block that may potentially slide or fall from the periphery of an underground excavation (Figure 4.44d). In the former case, dilation is permitted to occur freely, but in the latter case, dilation may be inhibited by the surrounding rock and the normal stress may increase with shear displacement.

When laboratory specimens in the configuration of Figure 4.44a are subjected to a shear stress, $\tau$, parallel to the discontinuity, they can undergo shear and normal

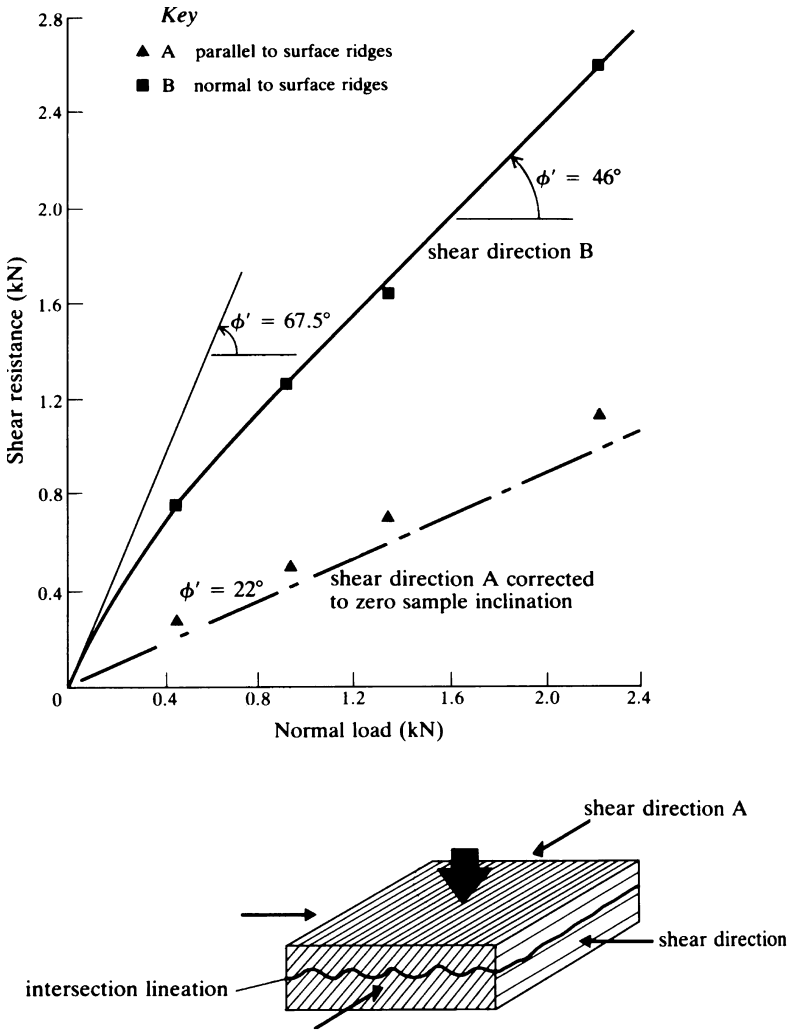


**Figure 4.43** Effect of shearing direction on the shear strength of a wet discontinuity in a slate (after Brown *et al.*, 1977).

displacements, $u$ and $v$, respectively. When a normal compressive stress, $\sigma_n$ is applied, the discontinuity will compress. This compressive stress–displacement behaviour is highly non-linear (Figure 4.45a) and at high values of $\sigma_n$, becomes asymptotic to a maximum closure, $V_{mc}$, related to the initial thickness or aperture of the discontinuity.

Suppose that a clean, rough discontinuity is sheared with no normal stress applied. Dilatancy will occur as shown in the upper curve of Figure 4.45b. If the shear resistance is assumed to be solely frictional, the shear stress will be zero throughout. For successively higher values of constant normal stress, *A, B, C* and *D*, the initial normal displacement will be *a, b, c* and *d* as shown in Figure 4.45a, and the dilatancy–shear displacement and shear stress–shear displacement curves obtained during shearing will be as shown in Figures 4.45b and c. As the normal stress is increased, the amount of dilatancy will decrease because a greater proportion of the asperities will be damaged during shearing.

Now suppose that a test is carried out on the same specimen with the normal stress initially zero and no dilation permitted during shearing (i.e. $v = 0$ throughout). By

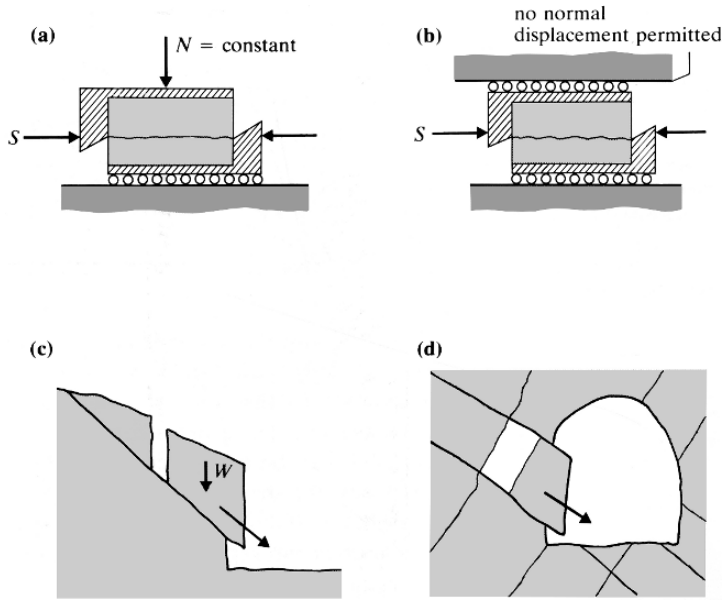


**Figure 4.44** Controlled normal force (a, c) and controlled normal displacement (b, d) shearing modes.

the time a shear displacement corresponding to point 1 in Figure 4.43b is reached, a normal stress of $\sigma_n = A$ will have been acquired, and the shear resistance will be that given by the $\tau$–$u$ curve for $\sigma_n = A$ at $u = u_1$. As shearing progresses, the shear stress will increase according to the dashed locus 0–1–2 in Figure 4.45c. If the discontinuity is initially compressed to point 3 in Figure 4.45b by a normal stress $\sigma_n = A$, and shearing then occurs with no further normal displacement being permitted (i.e. $v = a$ throughout), then the $\tau$–$u$ curve followed will be that given by the locus 3–4–5–6 in Figure 4.45c. Note that, in both cases, considerable increases in shear strength accompany shearing without dilatancy, and that the $\tau$–$u$ behaviour is no longer strain softening as it was for constant normal stress tests. This helps explain why limiting dilation on discontinuities by rock bolt, dowel and cable reinforcement (Chapter 11), can stabilise excavations in discontinuous rock.

### *4.7.4 Influence of scale*

As was noted in section 3.3, discontinuity roughness may exist on a number of scales. Figure 3.10 illustrated the different scales of roughness sampled by different scales of shear test. For tests in which dilation is permitted, the roughness angle and, therefore, the apparent friction angle, decrease with increasing scale. For tests in which dilation is inhibited, the influence of scale is less important.

Barton (1973) proposed that the peak shear strengths, of joints, $\tau$, in rock could be represented by the empirical relation

$$\tau = \sigma'_n \tan\left[JRC \log_{10}\left(\frac{JCS}{\sigma'_n}\right) + \phi'_r\right] \tag{4.35}$$

where $\sigma'_n$ = effective normal stress, $JRC$ = joint roughness coefficient on a scale of 1 for the smoothest to 20 for the roughest surfaces, $JCS$ = joint wall compressive strength and $\phi'_r$ = drained, residual friction angle.

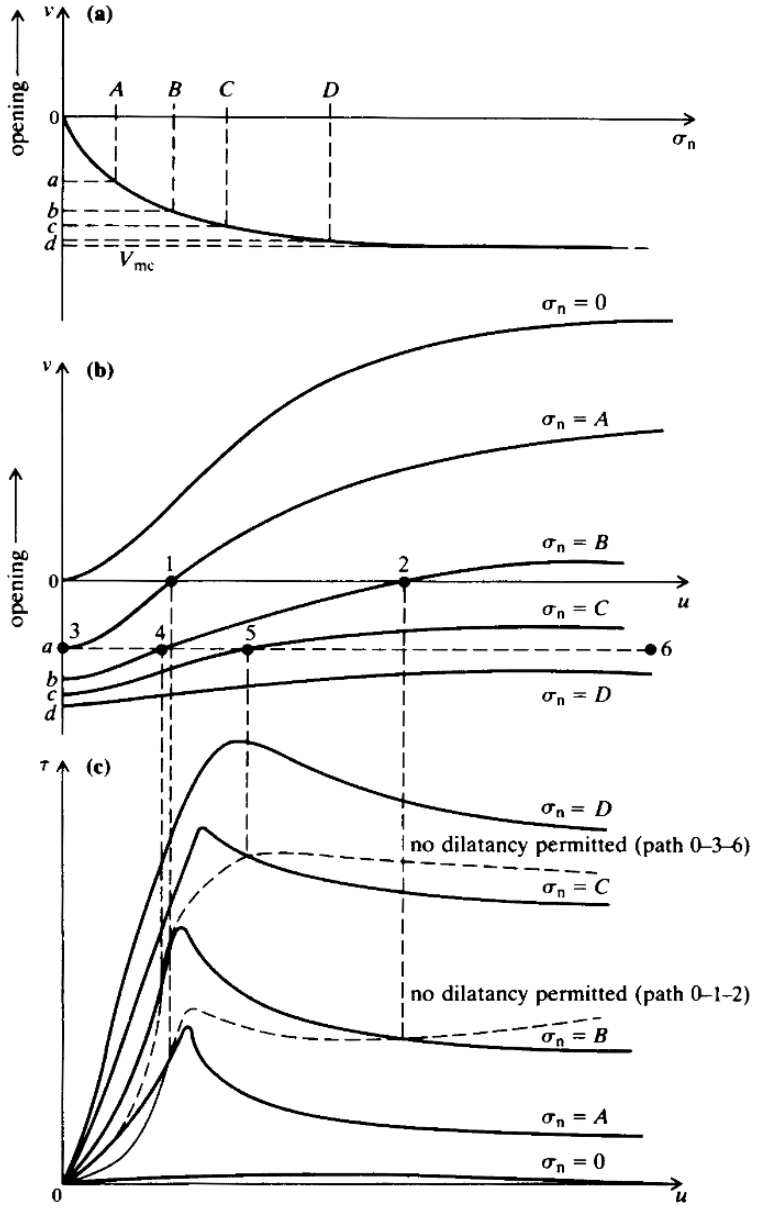


**Figure 4.45** Relations between normal stress ($\sigma_n$), shear stress ($\tau$), normal displacement ($v$), and shear displacement ($u$) in constant displacement shear tests on rough discontinuities (after Goodman, 1989).

Equation 4.35 suggests that there are three components of shear strength – a basic frictional component given by $\phi_r'$, a geometrical component controlled by surface roughness ($JRC$) and an asperity failure component controlled by the ratio ($JCS/\sigma_n'$). As Figure 4.46 shows, the asperity failure and geometrical components combine to give the nett roughness component, $i^\circ$. The total frictional resistance is then given by $(\phi_r' + i)^\circ$.

Equation 4.35 and Figure 4.46 show that the shear strength of a rough joint is both scale dependent and stress dependent. As $\sigma_n'$ increases, the term $\log_{10}(JCS/\sigma_n')$

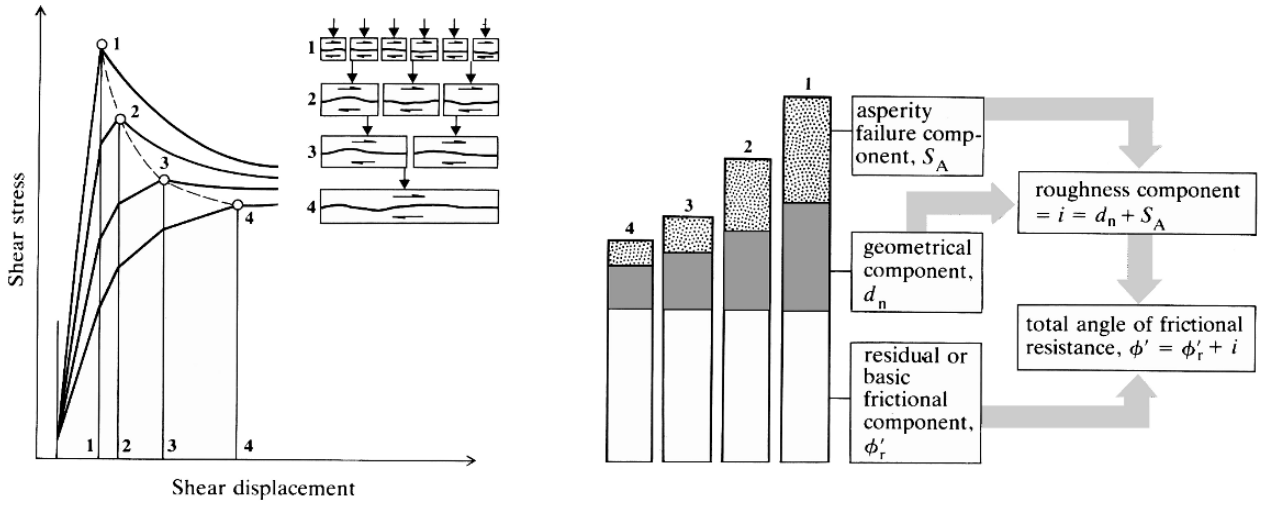


**Figure 4.46** Influence of scale on the three components of discontinuity shear strength (after Bandis *et al.*, 1981).

decreases, and so the nett apparent friction angle decreases. As the scale increases, the steeper asperities shear off and the inclination of the controlling roughness decreases. Similarly, the asperity failure component of roughness decreases with increasing scale because the material compressive strength, *JCS*, decreases with increasing size as discussed in section 4.3.5.

### *4.7.5 Infilled discontinuities*

The previous discussion referred to 'clean' discontinuities or discontinuities containing no infilling materials. As noted in section 3.3, discontinuities may contain infilling materials such as gouge in faults, silt in bedding planes, low-friction materials such as chlorite, graphite and serpentine in joints, and stronger materials such as quartz or calcite in veins or healed joints. Clearly, the presence of these materials will influence the shear behaviour of discontinuities. The presence of gouge or clay seams can decrease both stiffness and shear strength. Low-friction materials such as chlorite, graphite and serpentine can markedly decrease friction angles, while vein materials such as quartz can serve to increase shear strengths.

Of particular concern is the behaviour of major infilled discontinuities in which the infilling materials are soft and weak, having similar mechanical properties to clays and silts. The shear strengths of these materials are usually described by an effective stress Coulomb law. In a laboratory study of such filled discontinuities, Ladanyi and Archambault (1977) reached the following conclusions:

(a) For most filled discontinuities, the peak strength envelope is located between that for the filling and that for a similar clean discontinuity.
(b) The stiffnesses and shear strength of a filled discontinuity decrease with increasing filling thickness, but always remain higher than those of the filling alone.
(c) The shear stress–displacement curves of filled discontinuities often have two portions, the first reflecting the deformability of the filling materials before rock to rock contact is made, and the second reflecting the deformability and shear failure of rock asperities in contact.

(d) The shear strength of a filled discontinuity does not always depend on the thickness of the filling. If the discontinuity walls are flat and covered with a low-friction material, the shear surface will be located at the filling-rock contact.
(e) Swelling clay is a dangerous filling material because it loses strength on swelling and can develop high swelling pressures if swelling is inhibited.

## 4.8 Models of discontinuity strength and deformation

In section 4.7, discussion was concentrated on the factors influencing the peak and residual shear strengths of discontinuities. When the responses of discontinuous rock masses are modelled using numerical methods such as joint-element finite element or distinct element methods (Chapter 6) it is also necessary that the shear and normal displacements on discontinuities be considered. The shear and normal stiffnesses of discontinuities can exert controlling influences on the distribution of stresses and displacements within a discontinuous rock mass. Three discontinuity strength and deformation models of varying complexity will be discussed here. For simplicity, the discussion is presented in terms of total stresses.

### *4.8.1 The Coulomb friction, linear deformation model*

The simplest coherent model of discontinuity deformation and strength is the Coulomb friction, linear deformation model illustrated in Figure 4.47. Under normal compressive loading, the discontinuity undergoes linear elastic closure up to a limiting value of $\Delta v_m$ (Figure 4.47a). The discontinuity separates when the normal stress is less than the discontinuity tensile strength, usually taken as zero. For shear loading (Figure 4.47b), shear displacement is linear and reversible up to a limiting shear stress (determined by the value of the normal stress), and then perfectly plastic. Shear load reversal after plastic yield is accompanied by permanent shear displacement and hysteresis. The relation between limiting shear resistance and normal stress is given by equation 4.11.

This model may be appropriate for smooth discontinuities such as faults at residual strength, which are non-dilatant in shear. The major value of the model is that it provides a useful and readily implemented reference case for static discontinuity response.

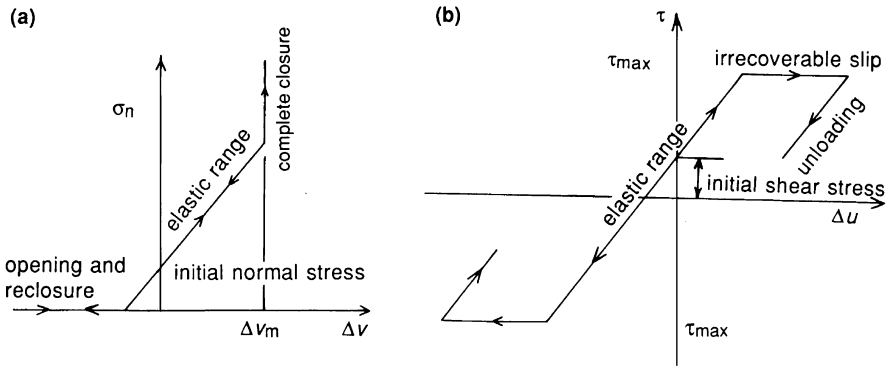


**Figure 4.47** Coulomb friction, linear deformation joint model; (a) normal stress ($\sigma_n$)–normal closure ($\Delta$v) relation; (b) shear deformation ($\tau$)–shear displacement ($\Delta u$) relation.

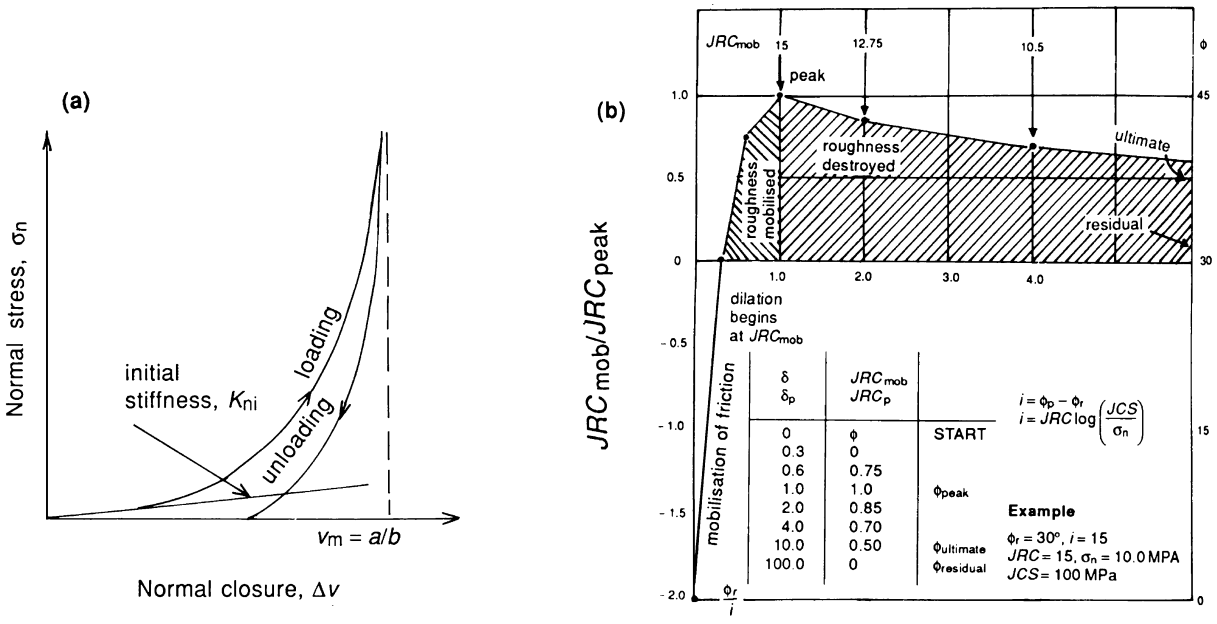


**Figure 4.48** The Barton–Bandis model: (a) normal stress–normal closure relation; (b) example of piecewise linear shear deformation simulation (after Barton *et al.,* 1985).

### *4.8.2 The Barton–Bandis model*

The data presented in section 4.7 expressed the non-linear nature of the mechanical responses of rough discontinuities in rock. The effects of surface roughness on discontinuity deformation and strength have been described by Bandis *et al.* (1983, 1985) and Barton *et al.* (1985) in terms of a series of empirical relations between stress and deformation components and the parameters joint roughness coefficient, JRC, and joint wall compressive strength, JCS, introduced in equation 4.35.

The Barton–Bandis discontinuity closure model incorporates hyperbolic loading and unloading curves (Figure 4.48a) in which normal stress and closure, $\Delta v$, are related by the empirical expression

$$\sigma_n = \Delta v/(a - b\Delta v) \tag{4.36}$$

where $a$ and $b$ are constants. The initial normal stiffness of the joint, $K_{ni}$, is equal to the inverse of $a$ and the maximum possible closure, $v_m$, is defined by the asymptote $a/b$.

Differentiation of equation 4.36 with respect to $\Delta v$ yields the expression for normal stiffness

$$K_n = K_{ni}[1 - \sigma_n/(v_m K_{ni} + \sigma_n)]^{-2}$$

which shows the normal stiffness to be highly dependent on normal stress.

To provide estimates of joint initial stiffness and closure, Bandis *et al.* (1985) present the empirical relations

$$K_{ni} = 0.02(JCS_0/E_0) + 2.0JRC_0 - 10$$
$$v_m = A + B(JRC_0) + C(JCS_0/E_0)^D$$

where $JCS_0$ and $JRC_0$ are laboratory scale values, $E_0$ is the initial aperture of the discontinuity, and $A$, $B$, $C$ and $D$ are constants which depend on the previous stress history.

The peak shear strength is given by equation 4.35. The gradual reduction in shear strength during post-peak shearing is caused by a decline in the effective contribution of roughness due to mismatch and wear. This behaviour is modelled by using different values for the roughness coefficient, $JRC_{\text{mob}}$, that will be mobilised at any given value of shear displacement, $u$. A set of empirical relations between $u$, $JRC$, $JCS$, $\sigma_n$, the mobilised dilation angle and the size of the discontinuity permits the shear stress–shear displacement curve to be modelled in piecewise linear form (Figure 4.48b).

The Barton–Bandis model takes explicit account of more features of discontinuity strength and deformation behaviour than the elementary model discussed in section 4.8.1. However, its practical application may present some difficulties. In particular, the derivation of relations for the mobilisation and degradation of surface roughness from a piecewise linear graphical format rather than from a well-behaved formal expression may lead to some irregularities in numerical simulation of the stress–displacement behaviour.

Although three decades of experience has been gained in assigning *JRC* values, the exercise remains a subjective one. A range of approaches to the measurement of *JRC* involving surface profiling and statistical and fractal analyses have been proposed. Grasselli and Egger (2003), for example, used an advanced topometric sensor (ATS) scanner to obtain digitised three-dimensional profiles of the surfaces of joints in seven rock types which were then subjected to constant normal load direct shear tests. As in the example shown in Figure 4.43, they found that the surface profiles and the associated shear strengths were anisotropic. They were able to fit the measured shear strengths to the peak shear strength criterion given by equation 4.35 using a model in which the value of *JRC* on the laboratory scale was expressed as a function of the basic friction angle, the ratios of uniaxial compressive and tensile strengths to the average normal stress, and a number of parameters which represent the three dimensional surface morphology of the joint and the direction of shearing.

### *4.8.3 The continuous-yielding joint model*

The continuous-yielding joint model was designed to provide a coherent and unified discontinuity deformation and strength model, taking account of non-linear compression, non-linearity and dilation in shear, and a non-linear limiting shear strength criterion. Details of the formulation of the model are given by Cundall and Lemos (1990).

The key elements of the model are that all shear displacement at a discontinuity has a component of plastic (irreversible) displacement, and all plastic displacement results in progressive reduction in the mobilised friction angle. The displacement relation is

$$\Delta u^{\text{p}} = (1 - F)\Delta u$$

where $\Delta u$ is an increment of shear displacement, $\Delta u^{\text{p}}$ is the irreversible component of shear displacement and $F$ is the fraction that the current shear stress constitutes of the limiting shear stress at the prevailing normal stress.

The progressive reduction in shear stress is represented by

$$\Delta\phi_m = -\frac{1}{R}(\phi_m - \phi_b)\Delta u^p$$

where $\phi_m$ is the prevailing mobilised friction angle, $\phi_b$ is the basic friction angle, and $R$ is a parameter with the dimension of length, related to joint roughness.

The response to normal loading is expressed incrementally as

$$\Delta\sigma_n = K_n \Delta v$$

where the normal stiffness $K_n$ is given by

$$K_n = \alpha_n \sigma_n^{\beta_n}$$

in which $\alpha_n$ and $\beta_n$ are further model parameters.

The shear stress and shear displacement increments are related by

$$\Delta\tau = F K_s \Delta u$$

where the shear stiffness may also be taken to be a function of normal stress, e.g.

$$K_s = \alpha_s \sigma_n^{\beta_s}$$

in which $\alpha_s$, $\beta_s$ are further model parameters.

The continuously-yielding joint model has been shown to have the capability to represent satisfactorily single episodes of shear loading and the effects of cyclic loading in a manner consistent with that reported by Brown and Hudson (1974).

## 4.9 Behaviour of discontinuous rock masses

### *4.9.1 Strength*

The determination of the global mechanical properties of a large mass of discontinuous *in situ* rock remains one of the most difficult problems in the field of rock mechanics. Stress–strain properties are required for use in the determination of the displacements induced around mine excavations, and overall strength properties are required in, for example, assessments of pillar strength and the extent of discontinuous subsidence.

A first approach to the determination of the overall strength of a multiply jointed rock mass is to apply Jaeger's single plane of weakness theory (section 4.6) in several parts. Imagine that a rock mass is made up of the material for which the data shown in Figure 4.33b were obtained, but that it contains four sets of discontinuities each identical to the cleavage planes in the original slate. The sets of discontinuities are mutually inclined at 45° as shown in the sketches in Figure 4.49. A curve showing the variation of the peak principal stress difference with the orientation angle, $\alpha$, may be constructed for a given value of $\sigma_3$ by superimposing four times the appropriate curve in Figure 4.33b with each curve displaced from its neighbour by 45° on the $\alpha$ axis. Figure 4.49 shows the resulting rock mass strength characteristics for three values of $\sigma_3$. In this case, failure always takes place by slip on one of the discontinuities. Note that, to a very good approximation, the strength of this hypothetical rock mass may

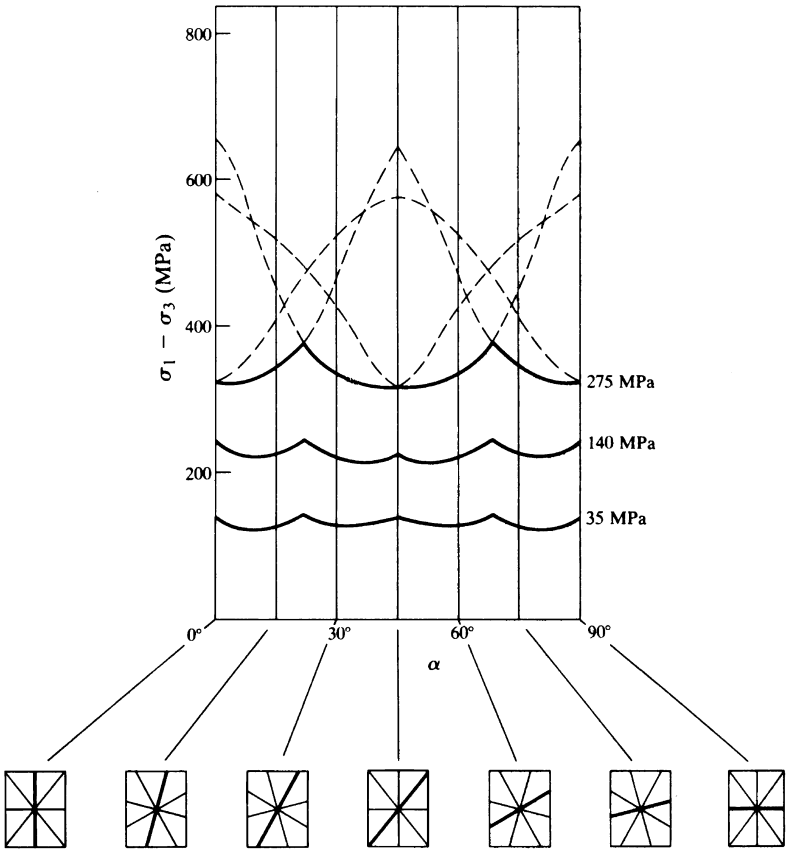


**Figure 4.49** Composite peak strength characteristics for a hypothetical rock mass containing four sets of discontinuities each with the properties of the cleavage in the slate for which the data shown in Figure 4.33b were obtained.

be assumed to be isotropic. This would not be the case if one of the discontinuity sets had a substantially lower shear strength than the other sets.

Because of the difficulty of determining the overall strength of a rock mass by measurement, empirical approaches are generally used. As discussed in section 4.5.5, Brady (1977) found that the power law of equation 4.23 could be applied to the mineralised shale at the Mount Isa Mine. An attempt to allow for the influence of rock quality on rock mass strength was made by Bieniawski (1976) who assigned Coulomb shear strength parameters, $c$ and $\phi$, to the various rock mass classes in his geomechanics classification (Table 3.5). Correlations have also been proposed between other rock mass classification schemes and rock mass strengths (e.g. Barton, 2002, Laubscher, 1990, Laubscher and Jakubec, 2001).

The most completely developed of these empirical approaches is that introduced by Hoek and Brown (1980). Because of a lack of suitable alternatives, the Hoek-Brown empirical rock mass strength criterion was soon adopted by rock mechanics practitioners, and sometimes used for purposes for which it was not originally intended and which lay outside the limits of the data and methods used in its derivation. Because of this, and as experience was acquired in its practical application, a series of changes were made and new elements introduced into the criterion. Hoek and Brown (1997) consolidated the changes made to that time and gave a number of worked examples to

illustrate the criterion's application in practice. A further update was given by Hoek *et al.* (2002). The summary of the criterion given here is based on these accounts and those of Marinos and Hoek (2000) and Brown (2003).

In effective stress terms, the generalised Hoek-Brown peak strength criterion for jointed rock masses is given by:

$$\sigma_1' = \sigma_3' + \left(m_b \sigma_c \sigma'_3 + s\sigma_c^2\right)^a \tag{4.37}$$

where $m_b$ is the reduced value of the material constant $m_i$ (see equation 4.25) for the rock mass, and $s$ and $a$ are parameters which depend on the characteristics or quality of the rock mass. The values of $m_b$ and $s$ are related to the GSI for the rock mass (see section 3.7.4) by the relations

$$m_b = m_i \exp\{(\text{GSI} - 100)/(28 - 14\text{D})\} \tag{4.38}$$

and

$$s = \exp\{(\text{GSI} - 100)/(9 - 3\text{D})\} \tag{4.39}$$

where $D$ is a factor which depends on the degree to which the rock mass has been disturbed by blasting or stress relaxation. $D$ varies from 0 for undisturbed *in situ* rock masses to 1.0 for very disturbed rock masses. For good quality blasting, it might be expected that $D \approx 0.7$.

In the initial version of the Hoek-Brown criterion, the index a took the value 0.5 as shown in equation 4.25. After a number of other changes, Hoek *et al.* (2002) expressed the value of a which applies over the full range of GSI values as the function:

$$a = 0.5 + (\exp^{-\text{GSI}/15} - \exp^{-20/3})/6 \tag{4.40}$$

Note that for GSI $> 50$, $a \approx 0.5$, the original value. For very low values of GSI, $a \rightarrow 0.65$.

The uniaxial compressive strength of the rock mass is obtained by setting $\sigma_3'$ to zero in equation 4.37 giving

$$\sigma_{cm} = \sigma_c s^a \tag{4.41}$$

Assuming that the uniaxial and biaxial tensile strengths of brittle rocks are approximately equal, the tensile strength of the rock mass may be estimated by putting $\sigma_1' = \sigma_3' = \sigma_{tm}$ in equation 4.37 to obtain

$$\sigma_{tm} = -s\,\sigma_c / m_b \tag{4.42}$$

The resulting peak strength envelope for the rock mass is as illustrated in Figure 4.50. Because analytical solutions and numerical analyses of a number of mining rock mechanics problems use Coulomb shear strength parameters rather than principal stress criteria, the Hoek-Brown criterion has also been represented in shear stress-effective normal stress terms. The resulting shear strength envelopes are non-linear and so equivalent shear strength parameters have to be determined for a given normal stress or effective normal stress, or for a small range of those stresses (Figure 4.50).

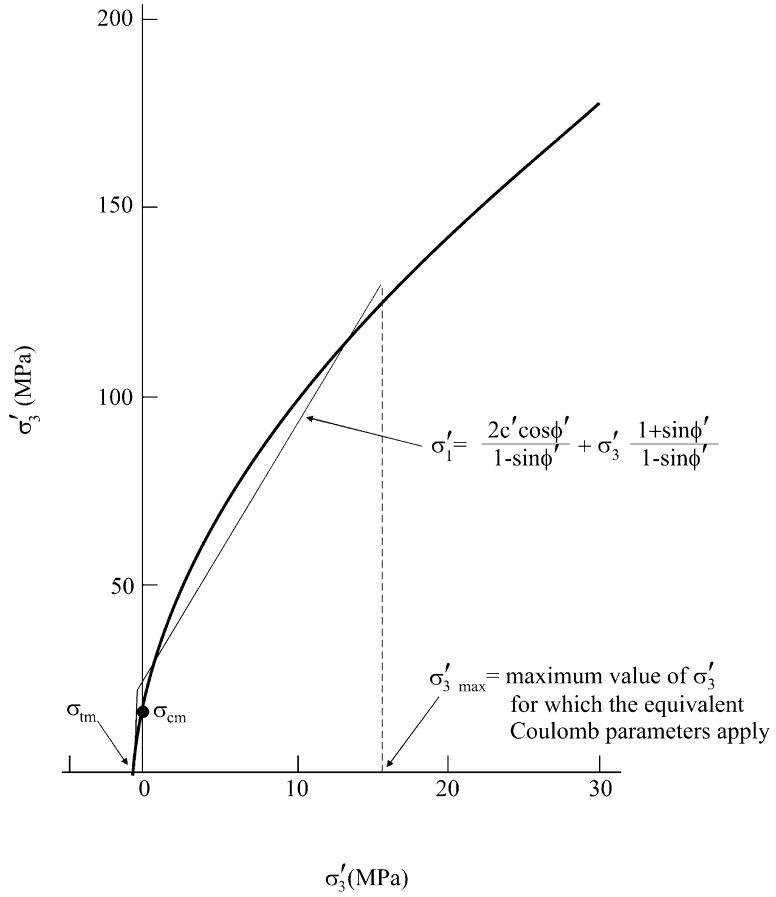


**Figure 4.50** Hoek-Brown peak strength envelope for a diorite rock mass with $\sigma_c = 100$ MPa, $m_i = 25$ and GSI 65 and the equivalent Coulomb shear strength parameters.

Methods of doing this are proposed by Hoek and Brown (1997), Hoek *et al.* (2002) and Sofianos (2003).

It is important to recognise that the Hoek-Brown rock mass strength criterion as presented here is a short-term peak strength criterion and not a crack initiation or long-term strength criterion. Furthermore, it applies only to sensibly isotropic rock masses as in the case illustrated in Figure 4.49. In particular, it should not be used when failure is governed by a single discontinuity or by a small number of discontinuities. The limitations of the criterion and the conditions under which it should be used have been discussed by Hoek and Brown (1997) and are illustrated in Figure 4.51.

### *4.9.2 Deformability*

The study of the complete stress–strain behaviour of jointed rock masses involving post-yield plastic deformation, is beyond the scope of this introductory text. However, it is of interest to consider the pre-peak behaviour with a view to determining equivalent overall elastic constants for use in design analyses.

In the simplest case of a rock mass containing a single set of parallel discontinuities, a set of elastic constants for an equivalent transversely isotropic continuum may be determined. For a case analogous to that shown in Figure 2.10, let the rock material

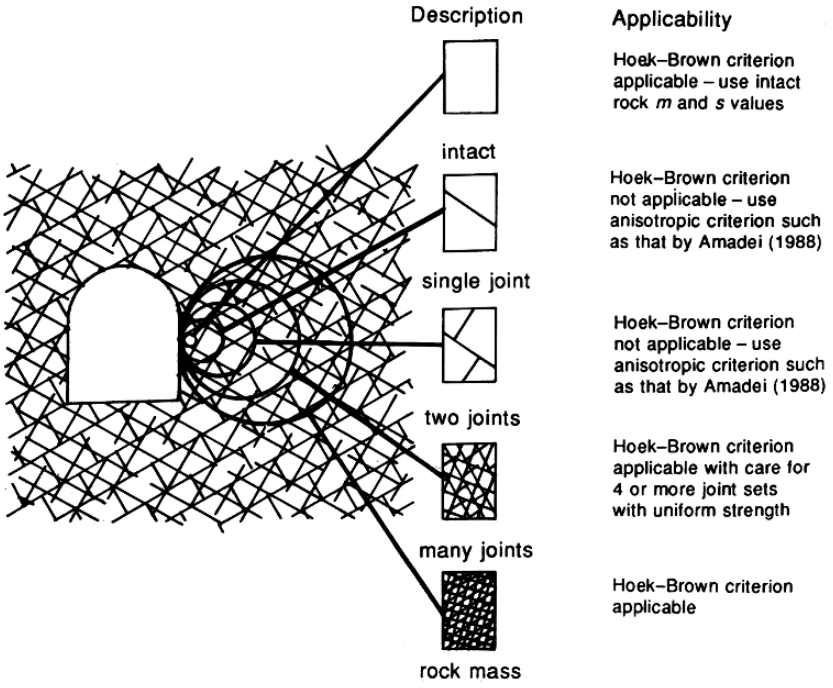


**Figure 4.51** Applicability of the Hoek–Brown empirical rock mass strength criterion at different scales (after Hoek and Brown, 1988).

be isotropic with elastic constants $E$ and $\nu$, let the discontinuities have normal and shear stiffnesses $K_n$ and $K_s$ as defined in section 4.7.5, and let the mean discontinuity spacing be $S$. By considering the deformations resulting from the application of unit shear and normal stresses with respect to the $x$, $y$ plane in Figure 2.10, it is found that the equivalent elastic constants required for use in equation 2.42 are given by

$$E_1 = E$$
$$\frac{1}{E_2} = \frac{1}{E} + \frac{1}{K_n S}$$
$$\nu_1 = \nu$$
$$\nu_2 = \frac{E_2}{E}\nu$$
$$\frac{1}{G_2} = \frac{1}{G} + \frac{1}{K_s S}$$

If, for example, $E = 10$ GPa, $\nu = 0.20$, $K_n = 5$ GPa m$^{-1}$, $K_s = 0.1$ GPa m$^{-1}$ and $S = 0.5$ m, then $G = 4.17$ GPa, $E_1 = 10$ GPa, $E_2 = 2.0$ GPa, $\nu_1 = 0.20$, $\nu_2 = 0.04$ and $G_2 = 49.4$ MPa.

Similar solutions for cases involving more than one set of discontinuities are given by Amadei and Goodman (1981) and by Gerrard (1982). It is often found in practice that the data required to apply these models are not available or that the rock mass structure is less regular than that assumed in developing the analytical solutions. In these cases, it is common to determine $E$ as the modulus of deformation or slope of the force–displacement curve obtained in an *in situ* compression test. There are

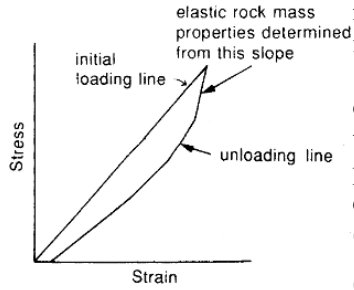


**Figure 4.52** Determination of the Young's modulus of a rock mass from the response on initial unloading in a cyclic loading test (after Brady *et al.*, 1985).

many types of *in situ* compression test including uniaxial compression, plate bearing, flatjack, pressure chamber, borehole jacking and dilatometer tests.

The results of such tests must be interpreted with care particularly when tests are conducted under deviatoric stress conditions on samples containing discontinuities that are favourably oriented for slip. Under these conditions, initial loading may produce slip as well as reflecting the elastic properties of the rock material and the elastic deformabilities of the joints. Using a simple analytical model, Brady *et al.* (1985) have demonstrated that, in this case:

(a) the loading–unloading cycle must be accompanied by hysteresis; and
(b) it is only in the initial stage of unloading (Figure 4.52) that inelastic response is suppressed and the true elastic response of the rock mass is observed.

Bieniawski (1978) compiled values of *in situ* modulus of deformation determined using a range of test methods at 15 different locations throughout the world. He found that for values of rock mass rating, RMR, greater than about 55, the mean deformation modulus, $E_M$, measured in GPa, could be approximated by the empirical equation

$$E_M = 2(\text{RMR}) - 100 \tag{4.43}$$

Serafim and Pereira (1983) found that an improved fit to their own and to Bieniawski's data, particularly in the range of $E_M$ between 1 and 10 GPa, is given by the relation

$$E_M = 10^{\frac{\text{RMR}-10}{40}} \tag{4.44}$$

Figure 4.53 shows equations 4.43 and 4.44 fitted to Bieniawski's (1978) and Serafim and Periera's (1983) data, respectively. It also shows further data provided by Barton (2002) fitted to the equation

$$E_M = 10\ Q_c^{1/3} \tag{4.45}$$

where $Q_c = Q\sigma_c/100$.

Following Hoek and Brown (1997), Hoek *et al.* (2002) proposed the more complex empirical relation

$$E_M = (1 - D/2)\sqrt{(\sigma_c/100)} \cdot 10^{((\text{GSI}-10)/40)} \tag{4.46}$$

which is derived from equation 4.44 but gives an improved fit to the data at lower values of RMR ($\approx$ GSI for RMR $> 25$), and includes the factor $D$ to allow for the effects of blast damage and stress relaxation.

It must be recognised that equations 4.43 to 4.46 relate rock mass classification indices to measured static deformability values that show considerable scatter. Accordingly, it cannot be expected that they will always provide accurate estimates of $E_M$. It must also be remembered that, as indicated earlier in this section, rock mass moduli may be highly anisotropic. They also vary non-linearly with the level of applied stress and so can be expected to vary with depth. Because of the high costs of carrying out *in situ* deformability tests, geophysical methods are often used to estimate *in situ* moduli. These methods generally involve studies of the transmission of

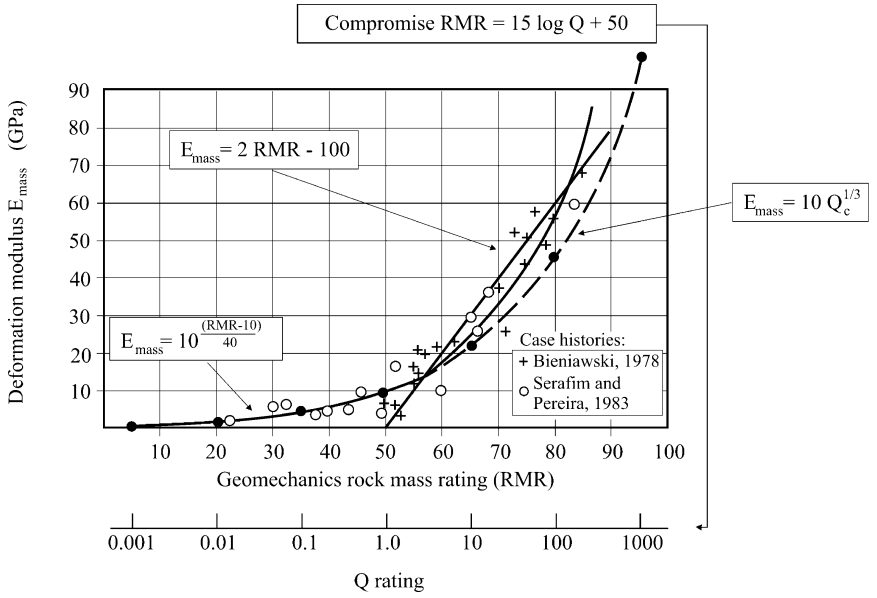


**Figure 4.53** Measured values of static rock mass modulus, $E_M$, and some empirical relations (after Barton, 2002).

elastic compression and shear waves through the rock mass and empirical correlations with rock mass classifications and dynamic and/or static moduli. Barton (2002), for example, was able to fit data from a number of hard rock sites using equation 4.45 with the value of $Q_c$ estimated from the *in situ* seismic P wave velocity, $V_p$(km s$^{-1}$), using the empirical relation

$$V_p \approx 3.5 + \log_{10} Q_c$$

## Problems

1 From the data given in Figure 4.18, calculate the tangent modulus and Poisson's ratio for the initial elastic behaviour of the limestone with $\sigma_3 = 2.0$ MPa.

2 A porous sandstone has a uniaxial compressive strength of $\sigma_c = 75$ MPa. The results of a series of triaxial compression tests plotted on shear stress–normal stress axes give a linear Coulomb peak strength envelope having a slope of 45°.

Determine the axial stress at peak strength of a jacketed specimen subjected to a confining pressure of $\sigma_3 = 10$ MPa. If the jacket had been punctured during the test, and the pore pressure had built up to a value equal to the confining pressure, what would the peak axial stress have been?

3(a) Establish an approximate peak strength envelope for the marble for which the data shown in Figure 4.19 were obtained.
3(b) In what ways might the observed stress–strain behaviour of the specimens have differed had the tests been carried out in a conventional testing machine having a longitudinal stiffness of 2.0 GN m$^{-1}$? Assume that all specimens were 50 mm in diameter and 100 mm long.

4 A series of laboratory tests on intact specimens of quartzite gave the following mean peak strengths. The units of stress are MPa, and compression is taken as positive.

| | $\frac{1}{2}(\sigma_1 + \sigma_3)$ | | $\frac{1}{2}(\sigma_1 - \sigma_3)$ |
|---|---|---|---|
| | 100 | | 100 |
| | 135 | | 130 |
| triaxial | 160 | | 150 |
| compression | 200 | | 180 |
| $\sigma_2 = \sigma_3$ | 298 | | 248 |
| | 435 | | 335 |
| | | | |
| | $\sigma_1$ | $\sigma_2$ | $\sigma_3$ |
| biaxial | 0 | 0 | −13.5 |
| tension/ | 0 | −13 | −13 |
| compression | 218 | 50 | 0 |
| | 225 | 100 | 0 |
| | 228 | 150 | 0 |
| | 210 | 210 | 0 |

Develop a peak strength criterion for the quartzite for use in underground excavation design. Experience has shown that the *in situ* uniaxial compressive strength of the quartzite is one-half the laboratory value.

5 A series of triaxial compression tests on specimens of a slate gave the following results:

| Confining pressure $\sigma_3$ (MPa) | Peak axial stress $\sigma_1$ (MPa) | Angle between cleavage and $\sigma_1$ $\alpha^\circ$ |
|---|---|---|
| 2.0 | 62.0 | 40 |
| 5.0 | 62.5 | 32 |
| 10.0 | 80.0 | 37 |
| 15.0 | 95.0 | 39 |
| 20.0 | 104.0 | 27 |

In each test, failure occurred by shear along the cleavage. Determine the shear strength criterion for the cleavage planes.

6 In a further series of tests on the slate for which the data of Problem 5 were obtained, it was found that, when failure occurred in directions other than along the cleavage, the peak strength of the rock material was given by

$$\sigma_1 = 150 + 2.8\sigma_3$$

where $\sigma_1$ and $\sigma_3$ are in MPa.

Construct a graph showing the expected variation of peak axial stress at a confining pressure of 10 MPa, as the angle between the cleavage and the specimen axis varies from $0^\circ$ to $90^\circ$.

7 The following results were obtained in a series of direct shear tests carried out on 100 mm square specimens of granite containing clean, rough, dry joints.

| Normal stress | Peak shear strength | Residual shear strength | Displacement at peak shear strength | |
|---|---|---|---|---|
| | | | Normal | Shear |
| $\sigma_n$ (MPa) | $\tau_p$ (MPa) | $\tau_r$ (MPa) | $v$(mm) | $u$(mm) |
| 0.25 | 0.25 | 0.15 | 0.54 | 2.00 |
| 0.50 | 0.50 | 0.30 | 0.67 | 2.50 |
| 1.00 | 1.00 | 0.60 | 0.65 | 3.20 |
| 2.00 | 1.55 | 1.15 | 0.45 | 3.60 |
| 3.00 | 2.15 | 1.70 | 0.30 | 4.00 |
| 4.00 | 2.60 | – | 0.15 | 4.20 |

(a) Determine the basic friction angle and the initial roughness angle for the joint surfaces.
(b) Establish a peak shear strength criterion for the joints, suitable for use in the range of normal stresses, 0–4 MPa.
(c) Assuming linear shear stress-shear displacement relations to peak shear strength, investigate the influence of normal stress on the shear stiffness of the joints.

8 A triaxial compression test is to be carried out on a specimen of the granite referred to in Problem 7 with the joint plane inclined at 35° to the specimen axis. A confining pressure of $\sigma_3 = 1.5$ MPa and an axial stress of $\sigma_1 = 3.3$ MPa are to be applied. Then a joint water pressure will be introduced and gradually increased with $\sigma_1$ and $\sigma_3$ held constant. At what joint water pressure is slip on the joint expected to occur? Repeat the calculation for a similar test in which $\sigma_1 = 4.7$ MPa and $\sigma_3 = 1.5$ MPa.

9 In the plane of the cross section of an excavation, a rock mass contains four sets of discontinuities mutually inclined at 45°. The shear strengths of all discontinuities are given by a linear Coulomb criterion with $c' = 100$ kPa and $\phi' = 30°$.

Develop an isotropic strength criterion for the rock mass that approximates the strength obtained by applying Jaeger's single plane of weakness theory in several parts.

10 A certain slate can be treated as a transversely isotropic elastic material. Block samples of the slate are available from which cores may be prepared with the cleavage at chosen angles to the specimen axes.

Nominate a set of tests that could be used to determine the five independent elastic constants in equation 2.42 required to characterise the stress–strain behaviour of the slate in uniaxial compression. What measurements should be taken in each of these tests?